



1

2 Tectonic controls on the formation and evolution of internally drained  
3 systems in the western Betics fold-and-thrust belt (S Spain)

4 Alejandro Jiménez-Bonilla (1), Manuel Díaz-Azpiroz (1), Miguel Rodríguez-Rodríguez  
5 (1), Juan Carlos Balanyá (1), Jose Luis Yanes (1), Inmaculada Expósito (1)

6 (1) Physical, Chemical and Natural Department, University Pablo de Olavide, Seville, Spain

7 Corresponding author: Alejandro Jiménez Bonilla [ajimbon@upo.es](mailto:ajimbon@upo.es)

8

#### Abstract

9 We analyse the drainage network in a depressed area within the western Betics fold-and-  
10 thrust belt (southern Spain) to investigate the Atlantic-Mediterranean water divide  
11 evolution after the Messinian Salinity Crisis (last 5 My). To do that, we made a hydro -  
12 geomorphic evaluation of streams and endorheic basins together with a detailed field-  
13 based analyses of post-Serravallian structural features. Results from the analysis of stream  
14 profiles and the application of SLk and  $\chi$  indexes showed that Mediterranean streams  
15 present a higher incision capacity than Atlantic streams, tributaries of the Guadalquivir  
16 river. Moreover, several rivers captures of Atlantic river watersheds and of endorheic  
17 basins have been described and quantified. Although the Atlantic-Mediterranean water  
18 divide will probably move NW-ward, endorheic basins will still endure, hosted in a  
19 depressed area located between two active transpressive zones (the Algonales-Badolatosa  
20 and Torcal shear zones). Our results confirm that active tectonics have reshaped the area  
21 more intensively than previously considered, and that this modification had significant  
22 hydrological implications.

23



24 Keywords: Surface uplift, shear zones, playa-lake,  $\chi$  index, water divide.

25

26

## 27 **1. Introduction**

28 The topography of active mountain belts results from the competing interplay  
29 between internal and external geodynamic controls. Thus, mantle convection, tectonics  
30 and isostasy interact with climate and surface processes to shape the evolving landscape  
31 of these regions (e.g., Bahadori et al., 2022, and references therein).

32 In this regard drainage networks are particularly sensitive to transient topographic  
33 signals, undergoing changes in stream long-profiles and flow-directions, as well as  
34 topological reshape of basins by means of stream captures or basin divisions.(e.g. Babault  
35 et al., 2012; Giletycz et al., 2015; Winterberg and Willett, 2019). Afterward, drainage  
36 networks equilibrium is achieved in relatively short time, from 1000 to 100,000 yr.,  
37 although the lithology, the climate or the watershed size may change this timespan  
38 (Whipple and Tucker, 1999; Korup, 2006).

39 It is for this reason that both qualitative and quantitative analysis of drainage systems  
40 have often been used for the characterization of active tectonics (e.g. Pérez-Peña et al.,  
41 2010; Azañón et al., 2015). Nevertheless, endorheic basins have been rarely analysed for  
42 such purpose, despite the fact that tectonics often governs topographic barriers that  
43 enclose such basins, both favouring their inception and conditioning their subsequent  
44 evolution. These internally drained systems are identified in a great variety of tectonic  
45 scenarios such as rift systems (Río Grande and East African Rifts; Repasch et al., 2017;  
46 Berry et al., 2019), foreland basins (Duero basin; Anton et al., 2014), intramontane basins



47 (Giano and Schiattarella, 2023) and contractional belts (Puna-Altiplano and Tibetan  
48 Plateau; Sobel et al., 2003). These endorheic basins usually host wetlands, playa-lakes  
49 and ponds that depend on their water balances to be ecologically functional. The ratio  
50 between the average flooded surface (AFS) and its watershed surface (W) is relevant in  
51 the endowment of the hydrological functioning of such ecosystems (Rodríguez-  
52 Rodríguez et al., 2012). Active tectonics may modify the watershed area, and, as a  
53 consequence, the absolute water input, which results in AFS variations (Jiménez-Bonilla  
54 et al., 2023).

55 In the case of the Betic chain of southern Spain, endorheic areas cover much of both the  
56 internal zones (Mather, 2000; Stokes et al. 2019), and the fold-and-thrust belt, as well as its  
57 transition to the foreland basin, since the Pliocene (Medina, 1991; Rodríguez-Rodríguez et al.,  
58 2009; 2012; Jiménez-Bonilla et al., 2023). Our case study focuses on a depressed area related to  
59 the current Atlantic-Mediterranean divide within the western Betics fold-and-thrust belt (Figs. 1  
60 and 2). This area is characterized by a particularly dense cluster of playa-lakes and ponds (e.g.  
61 Rodríguez-Rodríguez, 2007; Rodríguez-Rodríguez et al., 2016). Because of their location near  
62 the headwater of highly energetic Mediterranean rivers, their existence is often ephemeral (ca.  
63 1000 yrs.; Rodríguez-Rodríguez et al., 2016).

64 Before the Atlantic-Mediterranean water divide inception, this area included one of  
65 the upper Miocene Atlantic-Mediterranean corridors: the Guadalhorce gateway (Martín  
66 et al., 2001; 2014). During this age, shallow marine sediments deposited in this area,  
67 which are currently uplifted more than 100 m. a.s.l. The Guadalhorce gateway closure,  
68 which is not yet fully understood, contributed to the isolation of the Mediterranean Sea  
69 and the subsequent Messinian Salinity Crisis (MSC), responsible for the significant drop  
70 of the Mediterranean Sea level. Previous works have proposed that the huge erosion  
71 volume associated with this event was compensated by an isostatic rebound of the



72 Mediterranean watershed, thus uplifting the topographic relief associated with the post-  
73 Tortonian Atlantic-Mediterranean divide (Elez et al., 2016; 2020). Nevertheless, this  
74 assumption is not supported by the characterization of structures potentially compatible  
75 with this mechanism. Interestingly, the current Atlantic-Mediterranean divide, coincides  
76 with the NW-ward migrating front of the Betic fold-and-thrust belt, dominated in our  
77 study area by right-lateral transpression (Díaz-Azpiroz et al., 2014; Barcos et al., 2015;  
78 Jiménez-Bonilla et al., 2015). In this regard, it is worth noting that recent works have  
79 suggested that the permanence of the above mentioned playa-lakes seems to depend on  
80 the ongoing tectonic activity in the area (Rodríguez-Rodríguez et al., 2009; Jiménez-  
81 Bonilla et al., 2023).

82 Thus, our first, broad objective is to explore the nature of the main factors that control the  
83 evolution of the Atlantic-Mediterranean divide, as well as the inception and later development of  
84 the endorheic systems from the MSC to the Holocene. To do that, we zoom into this time frame  
85 to analyse in detail the evolution of the late Quaternary playa-lake systems: timing, reshaping and  
86 fluvial captures. We explore the drainage network of both exorheic and endorheic watersheds  
87 combining the characterization of streams (stream profile, stream length-gradient index and  $\chi$   
88 index) with the analysis of the change in both shape and distribution of endorheic systems. We  
89 combine these geomorphic tools with the kinematic analysis of the recent to active tectonic  
90 structures, and we estimated the differential post-Tortonian uplift.

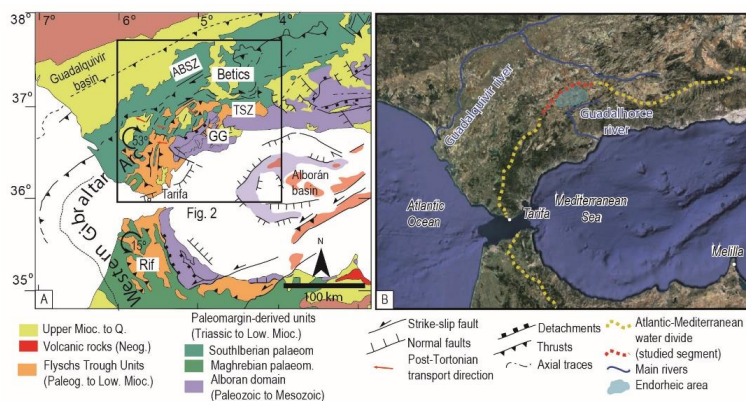
91

## 92 **2. Main geological and geomorphological features of the study area**

93 The Neogene collision between the Alboran domain and the Iberian and Maghrebian  
94 paleomargins built up the Gibraltar arc, which is composed of two branches: the Betics to the N  
95 and the Rif to the S (e.g., Vera, 2004; Fig. 1A). Between both paleomargins and the Alboran  
96 domain, Flysch Trough units were deposited. Both paleomargin-derived and Flysch units were



97 deformed into the Betics and Rif fold-and-thrust belts. At the concave side of the arc, a marine  
98 back-arc basin developed (Comas et al., 1999; Fig. 1A).



99

100

101 Fig. 1. (A) Tectonic map that shows the main structures (GG: Guadalhorce gateway) and (B)  
102 ortorphoto that includes the Atlantic-Mediterranean water divide and main rivers of the Betics  
103 chain (TSZ: Torcal Shear Zone; ABSZ: Algodonales-Badolatosa Shear Zone) © Google Earth  
104 image from 2021.

105

106 The Betics fold-and-thrust belt records two main deformation events: a lower to middle  
107 Miocene main deformation related to the external orogenic wedge accretion (Balanyá et al., 2007;  
108 Expósito et al., 2012) and a post-Serravallian deformation responsible for the current major relief  
109 features (Barcos et al., 2015; Jiménez-Bonilla et al., 2015; 2017). The post-Tortonian uplift is  
110 heterogeneous along and across the Betics, reaching the highest values (ca. 1,600 m) in the  
111 Eastern Betics, and more than 700 m in the Western Betics (Sanz de Galdeano and Alfaro, 2004;  
112 Jiménez-Bonilla et al., 2015; 2017).

113 During this post-Serravallian event, the second-order, the western Gibraltar arc became  
114 individualized as the westernmost salient of the Gibraltar arc (west of 4°30', Fig. 1). The  
115 individualization of the western Gibraltar arc has been accommodated in the northern branch, i.e.,



116 the Betics, by two dextral, transpressional shear zones (Jiménez-Bonilla et al., 2015; Díaz-  
117 Azpiroz et al., 2014; Barcos et al., 2015): the Torcal Shear Zone and the Algodonales-Badolatosa  
118 Shear Zone (TSZ and ABSZ, respectively; Fig. 2). This kinematics sharply contrast with that  
119 observed in the frontal part of the western Gibraltar arc, characterized by arc-parallel shortening  
120 structures and arc-perpendicular stretching structures (Balanyá et al., 2007; 2012; Jiménez-  
121 Bonilla et al., 2015; 2017; Figs. 1 and 2).

122         The post-Serravalian structures provoke a significant structural and topographic relief  
123 compartmentation where mountain ranges are interrupted by depressions along and across the  
124 fold-and-thrust belt (Fig. 2). Our study is focused on a roughly triangular depressed area, hereafter  
125 called as the Antequera Depressed Area (ADA), limited by the two above-mentioned post-  
126 Serravallian, dextral transpressive zones (Fig.2), located close to the contact with the Alboran  
127 domain.

128         The ADA shows a low-lying relief at about 400 m.a.s.l. and it is characterized by the  
129 development of endorheic basins since the Pliocene (Medina, 1991; Höbig et al., 2016). It is  
130 surrounded by areas rising over 100 m above this topographical depression, being the sharpest  
131 relief drops found in its NW, SE and SW boundaries (Fig. 2).

132         The ABSZ spatially coincides with the NW limit of the ADA. It is 90 km long and builds  
133 up SW-NE oriented mountain ranges that can be higher than 800 m (Fig. 2). It can be divided into  
134 three main segments, which are connected by NW-SE relay zones (Jiménez-Bonilla et al., 2015;  
135 Díaz-Azpiroz et al., 2020). To the SE of the ADA, the TSZ constitutes a 70 km long topographic  
136 high (up to 1,500 m), oriented approximately W-E (Fig. 2). The TSZ western segment (wTSZ in  
137 Figs. 2 and 3), has been interpreted as the tip zone of the TSZ. It consists of two WNW-ESE  
138 dextral strike-slip fault zones connected by a compressive bridge (Jiménez-Bonilla et al., 2013;  
139 Barcos et al., 2015).

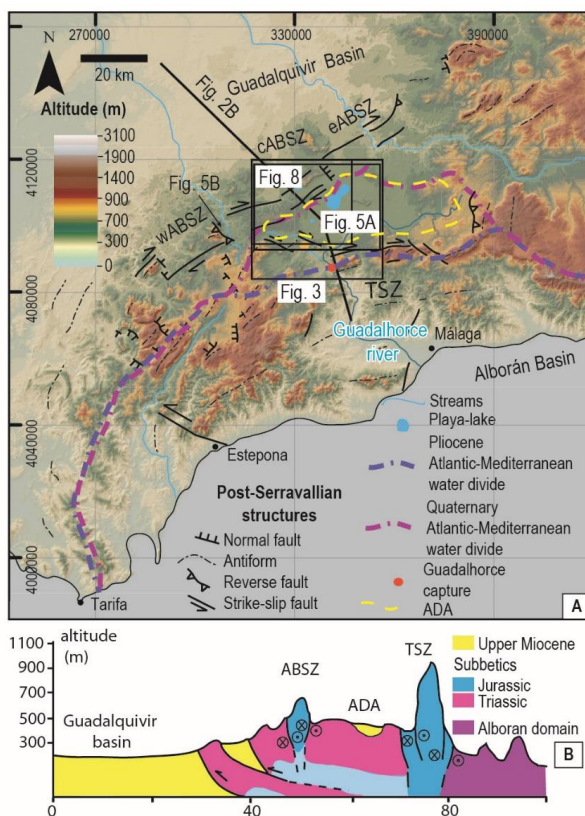
140         The rocks involved in our study area are mainly derived from the South-Iberian  
141 paleomargin. They belong to the Subbetic units (Vera et al., 2004), which are composed of: (1)



142 Triassic clays, gypsum and marls, with isolated hm-scale dolostone bodies, (2) Jurassic  
143 dolostones and limestones and (3) Cretaceous to Paleogene marls and marly-limestones that  
144 generally form isolated outcrops. Recent works have pointed out that the scarce hills that interrupt  
145 the ADA flat topography are controlled by pop-up structures that uplift Jurassic limestones  
146 underlain by a major allochthonous Triassic canopy (Flinch and Soto, 2017; 2022; Fig. 2B).  
147 Upper Miocene sediments unconformably lie over the Subbetic units (Martín et al., 2001; Fig.  
148 2B). Tortonian sedimentary rocks in the study area consists of calcirudites and calcarenites with  
149 shallow water fossils (pectinidae, ostreidae, sea urchins) and syn-sedimentary structures pointing  
150 to a moderate to high energetic deposition medium (cross bedding). Therefore, these formations  
151 may be a good proxy to the upper-Miocene sea level (Sanz de Galdeano and Alfaro, 2004).  
152 Continental sediments were deposited unconformably during the Pliocene to Quaternary.  
153 Pliocene sediments include clasts from the Alborán domain, located to the S. Quaternary deposits  
154 mainly correspond to alluvial terraces, associated with the main rivers, alluvial fans and  
155 pediments. Lacustrine dark quaternary sediments are well represented, being often useful to  
156 identify paleo playa lakes. Some of these outcrops are larger than 1,000 hm<sup>2</sup>.

157         The Quaternary Atlantic-Mediterranean water divide runs parallel to the Betics main  
158 trend. In the ADA, it is highly diffuse because of the presence, near the divide, of several  
159 endorheic systems (Fig. 2). The watersheds of these systems are located within the Atlantic or the  
160 Mediterranean watersheds. The Mediterranean and Atlantic watersheds are drained by  
161 Guadalhorce and Guadalquivir tributaries, respectively (Fig. 2).

162



163

164

165 Fig. 2. (A) Relief map of the western Betics showing the main post-Serravallian structures  
166 and the Atlantic-Mediterranean water divide in the Pliocene and in the Quaternary (Junta de  
167 Andalucía, 2016). (B) Geological cross-section across the western Betics that shows the main  
168 structures of the Betics fold-and-thrust belt. TSZ: Torcal Shear Zone; ABSZ: Algodonales-  
169 Badolatos Shear Zone; ADA: Antequera Depressed Area. See location in Fig. 1A.

170

### 171 3. Methodology

172 This work is an interdisciplinary study that combines structural and geomorphologic  
173 analyses, also including hydrogeological data and analytical modelling related to uplift.



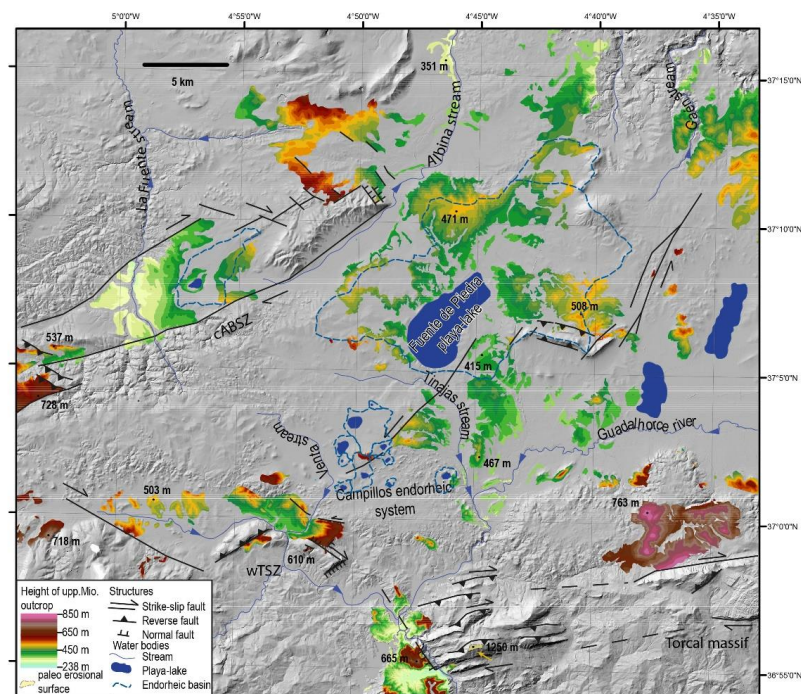
174 **3.1. Uplift estimates**

175 One of the main topics of this work is estimating the differential surface uplift from the  
176 Tortonian onwards and its possible linkage with upper Miocene deformation at specific shear  
177 zones. The former is obtained from a map that includes the current altitude of all marine, shallow  
178 water, upper-Miocene sediments in the study area (Fig. 3). The possible contribution of upper  
179 Miocene transpression at the TSZ to this differential uplift is evaluated by kinematic modelling.  
180 From a mathematical point of view, transpression is a combination of simple shearing parallel to  
181 the shear zone and a coaxial component that produces shortening across the shear zone and  
182 extrusion parallel to it (e.g., Sanderson and Marchini, 1984). Fernández et al. (2013) expanded  
183 the model of Schulmann et al. (2003) to calculate the vertical uplift  $U(dt)$  produced by coaxial  
184 extrusion in transpressive systems as follows:

$$\begin{aligned} 185 \quad U(dt) &= z(t_1) - z(t_0) = z(t_0) \delta [\sin^2 v + \cos^2 v \cdot \exp(\dot{\epsilon}t)] - z(t_0) = \\ 186 \quad & z(t_0) \{ \delta [\sin^2 v + \cos^2 v \cdot \exp(\dot{\epsilon}t)] - 1 \} \end{aligned} \quad (\text{Eq. 1})$$

187

188 where  $z(t_0)$  and  $z(t_1)$  are vertical distances to a reference level of zero extrusion (Rigid Floor Depth  
189 RFD, Schulmann et al., 2003) for times  $t_0$  and  $t_1$ , respectively;  $\delta$  is the true dip of the shear zone;  
190  $v$  is the angle between the extrusion direction of the coaxial component and the dip direction of  
191 the zone;  $\dot{\epsilon}$  is the coaxial strain rate and  $t$  is the time deformation has been acting (see Appendix  
192 A1 for a detailed reasoning).



193

194 Fig. 3. Hillshade map that shows the altitude of upper Miocene shallow marine outcrops in the  
195 study area and main post-Serravallian structures. The area includes the ADA (Antequera  
196 Depressed Area), the ABSZ and TSZ (Algodonales-Badolatosa Shear Zone and Torcal Shear  
197 Zone, respectively). It should be noted that the lowest altitudes are located within the ADA, whilst  
198 the highest ones are located close to the main shear zones. The map also shows Atlantic streams  
199 (Albuja, La Fuente and Gaén streams), Mediterranean streams (Venta, Guadalhorce and Tinajas  
200 streams) and main endorheic basins. See location in Fig. 2A (Junta de Andalucía, 2016).

201

### 202 3.2. Drainage network analyses and geomorphic indexes

203 For the analysis of the drainage network, we have interpreted key features of both the  
204 plan view geometry and the long profile of selected streams that cross the ABSZ. Within the  
205 Atlantic watershed, we have explored the Gaén stream, a Guadalquivir tributary that flows to the  
206 N (Figs. 2 and 3). Other Guadalquivir tributaries that have been studied in previous works have



207 been also added to our interpretation: La Fuente and Albina streams (Fig. 3; Jiménez-Bonilla et  
208 al., 2023). For the Mediterranean watershed, we have focused on the la Venta and Tinajas streams,  
209 which are tributaries of the Guadalhorce river, which finally discharges into the Mediterranean  
210 Sea (Figs. 2 and 3). We displayed post-Serravallian structures on stream profiles to investigate  
211 the relationship between knick-points and recent structures. To better identify knick-points, we  
212 used the Stream Length-gradient index (SL), but normalized by the graded river gradient (k): We  
213 applied the SLk index, which quantifies differences in the gradient on profiles generated to either  
214 lithological or tectonic contrasts (Pérez-Peña et al., 2009).

$$215 \quad SL = (dh/dl) * L \text{ (eq. 2)}$$

216 Where  $dh/dl$  is the slope and  $L$  the channel length. This index is normalized by  $k$ , graded  
217 river gradient:

$$218 \quad k = (C-hf) / \ln Lt \text{ (eq. 3)}$$

219 Where  $C$  is the river head elevation,  $hf$  elevation in the river mouth and  $Lt$  the total length  
220 (Pérez-Peña et al., 2009). We fixed a horizontal distance of 250 m.

### 221 **3.2.1. Analysis of playa-lakes and captures**

222 The Fuente Piedra playa-lake and the Campillos endorheic system are studied in relation  
223 to their drainage network evolution, geometric changes and stream captures, which are potentially  
224 controlled by active tectonics. To do that, we delimited the average flooded surface (AFS) and  
225 the endorheic watershed (W) using a 5-m DEM from Junta de Andalucía. Paleo watershed (p-W)  
226 can be delimited by the presence of knickpoints along stream profiles, which are used as a part of  
227 the water divide (Fig. 4A). However, p-W are sometimes measured indirectly by the relationship  
228 between W and AFS. AFS and W, together with the average runoff estimated in each location are  
229 related, such that we use the ratio  $W/AFS$  as an approximation to the water balance of playa-lakes  
230 (e.g. Rodríguez-Rodríguez et al., 2012). Most playa-lakes in the Betics present similar  $W/AFS$   
231 ratios (10-25), with slight variations attributed basically to differences in effective rainfall  
232 (ranging from 70 mm/year in the driest central part of Andalusia to 270 mm/year near the western



233 Atlantic coast) and to local factors such as human modifications of the W, suggesting these  
234 systems share their main controlling parameters: permeability of the substrate, climatology and  
235 average runoff (Rodríguez-Rodríguez et al., 2007). Assuming a constant climate, W/AFS ratio  
236 should be maintained for each playa-lake. The DEM also allowed us to delimitate the paleo-  
237 Average Flooded Surface (p-AFS) of several playa-lakes that have reduced their size and even of  
238 those that are currently desiccated (Fig. 4A). Because of the flat topography of the playa-lakes,  
239 we have identified such p-AFS as a flat surface currently perched over the recent AFS. Once the  
240 p-AFS is calculated, the size of the p-W can be easily estimated.

### 241 **3.2.2. $\chi$ index and divide migrations**

242 Additionally, the Atlantic-Mediterranean water divide stability has been evaluated by  
243 means of the  $\chi$  index, which permits to predict water divide movements by comparing the shape  
244 of streams long profiles situated on both sides of the water divide (Harkins et al., 2007; Perron  
245 and Royden, 2013; Willett et al., 2014).  $\chi$  maps yield a measurement of the disequilibrium of  
246 stream channels in opposite basins respecting a divide given that the  $\chi$  index depends inversely to  
247 the drained area. The  $\chi$ -transformed profile of a river is defined by the following equation when  
248 uplift rate (U) and erodibility (K) in time and space are considered as constant:

$$249 \quad z(x) = z_b(x_b) + \left(\frac{U}{K A_0^m}\right)^{1/n} \chi \quad (\text{eq. 4})$$

250 With

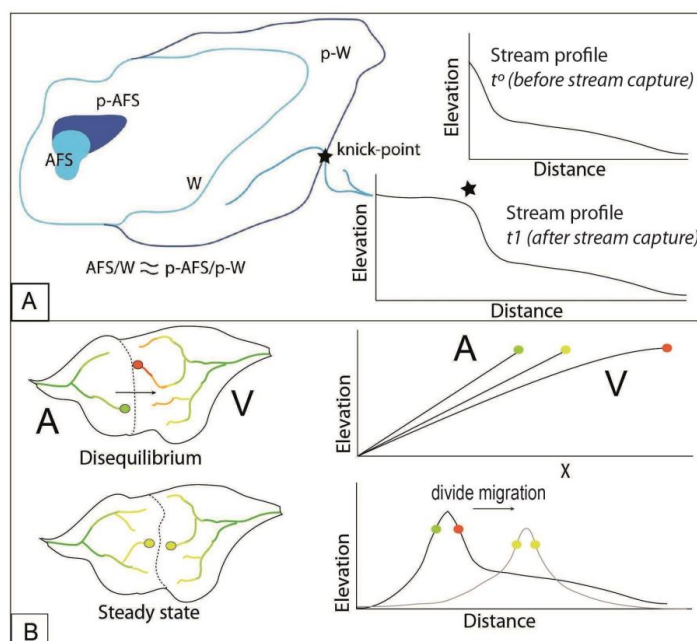
$$251 \quad \chi = \int_{x_b}^x \left(\frac{A_0}{A(x)}\right)^{m/n} dx \quad (\text{eq. 5})$$

252 where  $z(x)$  is the elevation of the channel,  $x$  is the longitudinal distance,  $z_b$  is the elevation  
253 at the river's base level (distance  $x_b$ ),  $A$  is the drainage area,  $A_0$  is a reference drainage area, and  
254 exponents  $m$  and  $n$  are empirical constants.

255 Thus,  $\chi$  mapping allows us to elucidate divide migrations when  $\chi$  is compared across  
256 drainage divides: similar values on both sides of the divide suggest that two opposite streams are



257 near equilibrium. If not, the stream with larger  $\chi$  value for a given altitude tend to be captured by  
258 basins with lower  $\chi$  (Willett et al., 2014; Fig. 4B). We made a  $\chi$  map for the study area and we  
259 considered the discharge point at the sea level.



260

261

262 Fig. 4. (A) Methodology applied to study the evolution of playa-lake systems (AFS: Area  
263 Flooded Surface; p-AFS (paleo-Area Flooded Surface). (B) Diagrams of  $\chi$  map showing the  
264 drainage network evolution when the water divide is in disequilibrium, stream profiles in  $\chi$  space  
265 and water divide profiles changes from a disequilibrium to a steady state (A: Stream aggressor  
266 and V: Stream victim). Modified from Willett et al., 2014.

267

#### 268 4. Results I: Post-Serravallian structures

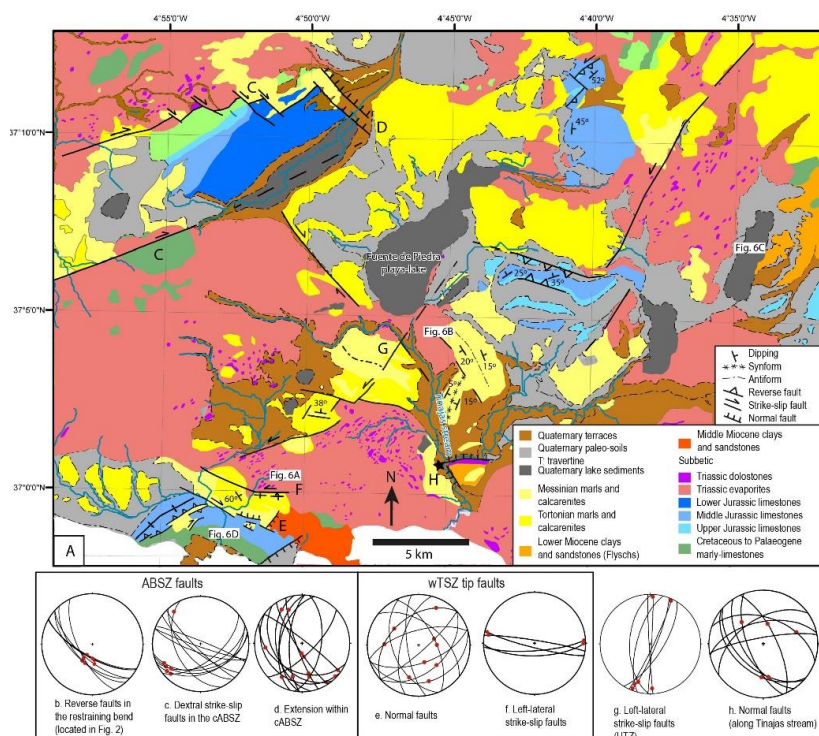


269           On the basis of previous works on the structure and kinematics of the TSZ and ABSZ, we  
270   have completed the structural record of these shear zones in the study area (Fig. 5). Additionally,  
271   we include for the first time kinematic data within the ADA.

272

273           **4.1. Structures related to main shear zones (the ABSZ and the**  
274           **TSZ)**

275           Our new structural data from the ABSZ come from the central ABSZ segment, which is  
276   the N boundary of the ADA (Figs. 2 and 3). To the SW, the central ABSZ oversteps the western  
277   ABSZ segment, being both linked by a restraining bend characterized by NW-SE oriented reverse  
278   faults (Figs. 5A and 5B). All these structures limit and deform WSW-ENE elongated sedimentary  
279   depocenters, upper Miocene to Quaternary in age (Figs. 3 and 5A). The deformation within the  
280   central ABSZ is partitioned into: (1) WSW-ENE to SW-NE dextral-normal faults (Fig. 5C)  
281   dipping up to 80° to the SE, (2) NW-SE dextral faults (Fig. 5C) interpreted as Riedel, which are  
282   particularly localized between the central and the eastern ABSZ.



283

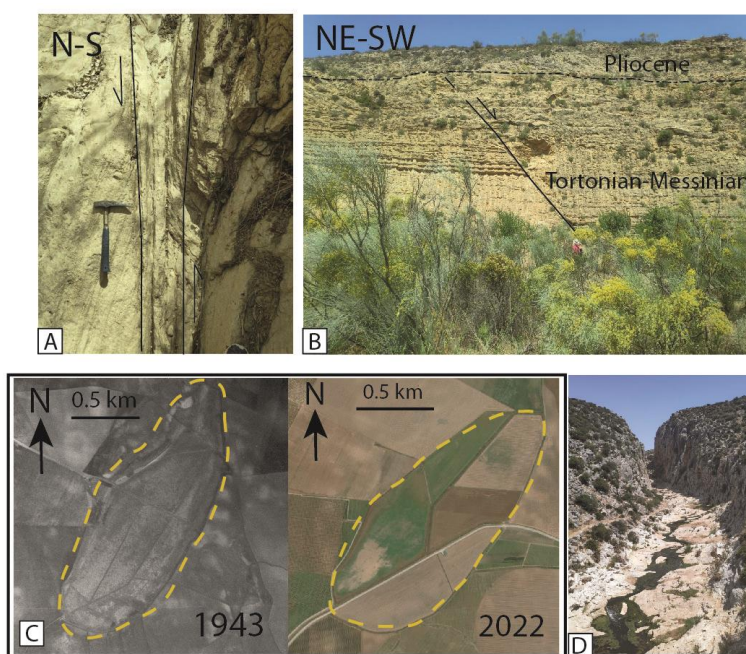
284 Fig. 5. (A) Geological map of the study area showing the main post-Serravallian  
 285 structures of the ADA, the central ABSZ and the wTSZ. See Fig. 2A for location. (B), (C) and  
 286 (D) Stereoplots related to structures of the ABSZ. (E) and (F) Stereoplots of structures in the W  
 287 tip of the TSZ. (G) and (H) Stereoplots of structures within the ADA (Modified from Jiménez-  
 288 Bonilla et al., 2023).

289

290 Within the TSZ, we collected new data from structures that deform the upper Miocene  
 291 rocks located in the western TSZ (Figs. 3 and 5). At this site, Miocene rocks are gently folded by  
 292 km-scale, WNW-ESE folds, and their limits are significantly determined by faults. Thus, normal  
 293 faults often developed in the contact between the Miocene rocks and the Jurassic limestones  
 294 (western TSZ, Figs. 3 and 5) as well as in its SE limit. They are defined, respectively, by WNW-  
 295 ESE and NE-SW fault planes that usually dip between 50° and 80° (Figs. 5A and E). The high  
 296 pitch of slickenlines (>60°) together with kinematic indicators, such as S-C structures, show a



297 dominant normal dip-slip component. The WNW-ESE fault system also hosts Miocene rocks  
298 within grabens surrounded by Jurassic limestones. The NE boundary of the Miocene outcrop is  
299 controlled by steeply dipping, WNW-ESE left lateral faults, interpreted as a positive transpressive  
300 flower structure because of the subordinate reverse-slip component (Figs. 5F and 6A). The  
301 bedding within its deformation zone is nearly vertical or even overturned up to  $60^\circ$  (Fig. 5A).  
302 Gentle slickenlines pitch angles, lower than  $10^\circ$ , together with kinematic indicators show a left-  
303 lateral strike-slip movement (Figs. 5F and 6A). This fault zone also involves Jurassic limestones.



304  
305 Fig. 6. Pictures of (A) vertical view of a left-lateral strike-slip fault zone that affect upper-  
306 Miocene rocks in the wTSZ, (B) a normal fault sealed by Pliocene sediments within the ADA,  
307 (C) aerial photographs to show the disappearance of a playa-lake due to human modifications  
308 (playa-lake is shown by discontinuous yellow line). PNOA images from 1943 and 2022 and (D)  
309 picture of the Venta stream deeply incised into the bed rock when it crosses the wTSZ. See  
310 location on Fig. 5A.

311



## 312           **4.2. Structures within the ADA**

313           In the ADA, Jurassic limestones crop out as tectonic windows in scattered topographic  
314           highs (Fig. 5A). Moderately deformed upper Miocene rocks overlie Jurassic limestones and  
315           Triassic evaporites and claystones. The deformation observed in upper Miocene rocks within the  
316           ADA is less pervasive than in the TSZ and the ABSZ and it is localized in deformation bands.

317           The main post-Serravallian structure is a transverse zone formed by three different  
318           segments: two NNE-SSW left-lateral strike-slip fault zones linked by a WNW-ESE restraining  
319           bend (Fig. 5A). NNE-SSW deformation bands are more than 2 km long. They form semi-brittle,  
320           damage zones, more than 1 km wide, where they affect Triassic clays and evaporites, whilst they  
321           develop as discrete faults where they affect competent rocks (i.e. Jurassic limestones; Fig. 5A).  
322           Within the damage zones, dolostones bodies reorientate their long-axis to become parallel with  
323           the fault zone, as it occurs in other deformation bands within Triassic rocks (e.g. in the eastern  
324           ABSZ; Díaz-Azpiroz et al., 2020; Fig. 5A). Fault planes within the damage zones are highly  
325           dipping and slickenlines between 5° and 20° (Fig. 5G) indicates a dominant lateral movement.  
326           The western fault zone constitutes the SE boundary of the Fuente de Piedra playa-lake basin and  
327           separates it from another small playa-lake to the E, which is at the uplifted block in this sector  
328           (Fig. 5A). The restraining bend between both sinistral fault zones develops as a pop-up structure  
329           uplifted by WNW-ESE, kilometric-scale tight folds and NNE/SSW-dipping fault planes. Its  
330           eastern tip is dragged by the western sinistral fault zone (Fig. 5A). Some of the faults related to  
331           this transverse zone affect quaternary sediments.

332           In addition to the transverse zone, some dip-slip dominated, normal faults affect upper-  
333           Miocene and younger formations. These faults are not concentrated in long fault zones, but they  
334           are usually discrete faults up to 1 km long (Fig. 5A). Vertical throw related to these faults is  
335           estimated to be smaller than 200 m using upper Miocene markers. These faults show two  
336           orientations: NW-SE faults that throw down the SW block and WSW-ENE faults that descend  
337           the N block. Slickenlines show pitch angles higher than 45° and, together with kinematic



338 indicators such as slickenfibers or S-C-like structures, indicate the downthrow of their hanging  
339 wall (Fig. 5H). The Fuente de Piedra playa-lake is in the N downthrown block of one of these  
340 WSW-ENE faults (Figs. 5A).

341 Additionally, some hm-hectometric-scale, open folds (interlimb angle larger than 120°)  
342 have been locally recognized (Fig. 5A). They are non-cylindrical folds, and their fold axis (NNW-  
343 SSE to NNE-SSW) are oblique to the Betic local regional orogenic grain (i.e., WSW-ENE).

344

## 345 **5. Results II: Estimates of post-Tortonian differential surface uplift**

346 As shown in section 4, faulting involves Tortonian formations. Additionally, these  
347 formations show noticeable altitude differences between the ABSZ, TSZ and the ADA, (from 250  
348 m a.s.l to 850 m a.s.l.; Fig. 3). Main features are as follow:

349 (1) Upper Miocene deposits altitude varies generally between 450 and 550 m along the  
350 ABSZ. The highest altitudes are found in the restraining bend between the central ABSZ  
351 and the western ABSZ (728 m a.s.l.; Figs. 2A, 3 and 5B).

352 (2) In the TSZ, these sediments are located between 550 and 850 m. In the TSZ western  
353 segment, the highest altitudes are found in those affected by left-lateral strike-slip faults  
354 that build up a positive flower (up to 610 m a.s.l.; Figs. 3, 5A, 5F and 6A). Towards the  
355 E, in the central segment (north of the TSZ, see Fig. 3 for location), these deposits reach  
356 their maximum altitudes within this shear zone (850 m a.s.l.). A paleo erosional surface  
357 dated as upper Miocene (Lhénaff, 1977) is correlated with this Tortonian sea level and  
358 located at 1,200 m a.s.l. (Barcos et al., 2015; Fig. 3).

359 (3) The highest altitudes in the ADA are found in the restraining bend of the above-described  
360 transverse zone (upper Miocene sediments up to 500 m a.s.l.), whereas undeformed areas  
361 would be at 350 m a.s.l. (Fig. 3).

362 Therefore, the post-Tortonian differential surface uplift (in the sense of England and Molner,  
363 1990) at the main shear zones compared to the endorheic basins in the less deformed areas would



364 reach around 200 m at the ABSZ, whereas at the TSZ is more than 350 m. Considering their  
365 spatial relationship and differences on Tortonian deposits altitude, we hypothesize that the recent  
366 deformation at these two shear zones is responsible for the observed differential uplift.

367 To test this hypothesis, we estimated the theoretical surface uplift produced by post-  
368 Tortonian transpressional deformation at the TSZ, following the approach of Schulmann et al.  
369 (2003) and Fuentes et al. (2019). The data needed for these calculations were obtained from  
370 previous detailed studies on the kinematics of this shear zone (Díaz-Azpiroz et al., 2014; Barcos  
371 et al., 2015) and are presented as follows (see also Table 1): (1) According to geophysical data,  
372 the base of the Triassic layer, where the main detachment (i.e., rigid floor depth, RFD, in  
373 Schulmann et al., 2003) would be located, is between 4500 and 6000 m (see also Medialdea et  
374 al., 1986 and Torné et al., 1992). We assume that the vertical distance of the analyzed formations  
375 to the RFD at the onset of deformation  $z(t_0)$  equals these values. (2) The true dip of the shear zone  
376 ( $\delta$ ) is 73°N. (3) Coaxial deformation is assumed to be pure shear and the extrusion angle ( $\nu$ ) is 0°  
377  $\pm 5^\circ$ , thus we consider up-dip pure shear ( $\nu = 0^\circ$ ), such that Eq. 2 simplifies to the Schulmann et  
378 al (2003) specific case:

379

$$380 \quad U(dt) = z(t_0) [(\dot{\epsilon}t) - 1] \quad (\text{Eq. 6})$$

381

382 The pure shear strain rate ( $\dot{\epsilon}$ ) is obtained from the total contraction accommodated orthogonally  
383 to the shear zone along a specific time interval ( $t$ )  $e = \frac{\dot{\epsilon}}{t}$ , which results in  $\dot{\epsilon} = e t$ . The onset of  
384 transpressional deformation at the TSZ needs to be younger than chevron folds that affected  
385 Upper Cretaceous-Paleogene reddish marly limestones of the Subbetic units, since these are  
386 interfered by transpressional structures (Díaz-Azpiroz et al., 2014). The age of these folds spans  
387 from 20.4 Ma (Aquitania-Burdigalian boundary), since the youngest deposits affected by these  
388 folds are Aquitanian in age, to 11.6 Ma (Serravalian-Tortonian boundary; Expósito et al., 2012).  
389 The total contraction produced at the inner domain of the Torcal de Antequera massif of the TSZ



390 along this interval ranges from 0.2 (obtained from cross-sections) to 0.27 (calculated from  
391 asymmetrical fold geometry). From these values, the resulting average pure shear strain rate  
392 related to transpression that acted in the TSZ in the last 11.6-20.4 my ranges between  $3.2 \cdot 10^{-16}$   
393  $s^{-1}$  and  $7.4 \cdot 10^{-16} s^{-1}$ . (4) The transpressional deformation that affected the upper Miocene  
394 calcirudites and calcarenites should have begun after the Tortonian, say in the Tortonian-  
395 Messinian transit, 7.3 my ago. If we assume the strain rate remains roughly constant, we can  
396 calculate the total contraction ( $e$ ), which is equivalent to the product  $\dot{\epsilon} t = 0.07 - 0.17$ . By  
397 substituting all these data into Eq. 2, we obtained the range of the tectonic uplift  $U(dt)$  due to  
398 transpressional deformation at the TSZ in the last 7.3 my (167 - 868 m, Table 1 and Fig. 7),  
399 depending on the RFD depth and the total contraction ( $e$ ). Our differential uplift estimations based  
400 on the current altitudes of the post-Tortonian marine sediments are better reproduced considering  
401 a total contraction value ( $e$ ) between 0.09 and 0.11 (for any RFD value). Different combinations  
402 of RFD with  $e = 0.07-0.09$  (large RFD) or  $e = 0.11-0.15$  (small RFD) may also produce reasonable  
403 correlations. Contraction values larger than 0.15 or lower than 0.07 would not explain the  
404 observed uplift results.

405

406 Table 1. Input data used for the modelling of post-Tortonian tectonic uplifting due to transpression  
407 at the TSZ (from Díaz-Azpiroz et al., 2014 and Barcos et al., 2015) and results of this model.  $z(t_1)$   
408 is the vertical distance to the RFD for time  $t_1$  (after deformation) and  $U(dt)$  is the corresponding  
409 uplift. See the main text for further details.

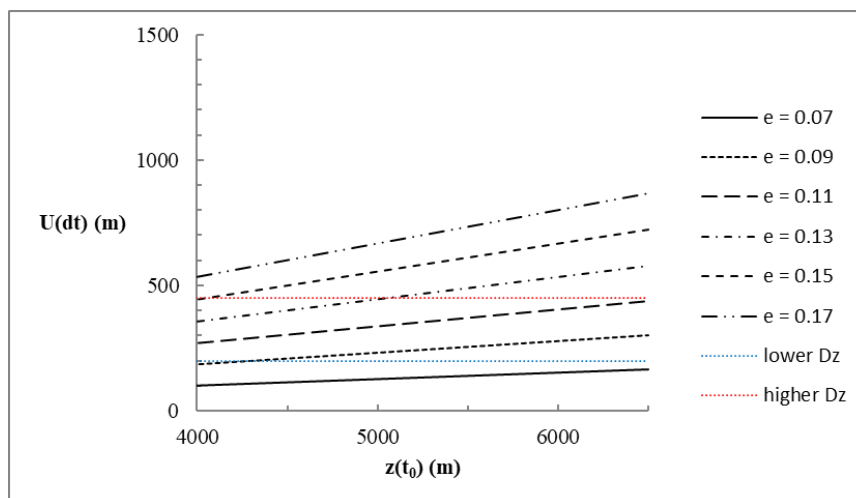
Factor	Input data
$z(t_0)$	4500 – 6000 m
$\delta$	73°
$\nu$	0°



$\dot{\epsilon}$	$3.2 \cdot 10^{-16} - 7.4 \cdot 10^{-16} \text{ s}^{-1}$
$t$	7.3 my
$e = \dot{\epsilon}t$	0.07 – 0.17
<hr style="border: 1px solid black;"/>	
<b>Results</b>	
$z(t_1)$	4615 – 7368 m
$U(dt)$	167 – 868 m
<hr style="border: 1px solid black;"/>	

410

411



412

413 Fig. 7. Theoretical post-Tortonian tectonic uplift due to the coaxial component of  
 414 transpressional deformation at the TSZ versus the RFD for different possible total contraction  
 415 values ( $e$ ), as calculated from kinematic models. The range of differential uplift measured between  
 416 the current altitude of Tortonian deposits at the TSZ and at the neighbouring undeformed area  
 417 ( $Dz$ ) is also shown for comparison.

418



419 **6. Results III: Geomorphic results**

420 Geomorphic results are derived from the analysis of streams (stream long profile together  
 421 with SLk index) that drain part of the ADA and flow to the Mediterranean Sea or to the Atlantic  
 422 Ocean (Figs. 1 and 2) or the playa-lakes located at the centre of some endorheic areas (Figs. 8 and  
 423 9). Table 2 compiles the information of changes of AFS and watersheds area and the relationships  
 424 between both. We have identified 17 endorheic basins with playa-lakes at their centre that  
 425 developed during the last 3,000 years. Three of them (numbers 14, 15 and 16 in Table 2) were  
 426 discarded from the analysis because their water balances are influenced by human modifications  
 427 of the AFS and W, such as drainages (AFS) and/or the construction of roads through them (W).

428

429 Table 2. Watershed (W), Average Flooded Area (AFS) and the W/AFS relationship of  
 430 the 17 endorheic basins detected in the studied area currently and in the past (p-W, p-AFS and  
 431 pW/AFS). Playa-lakes are located in Fig. 9 by numbering.

	W	AFS	W/AFS	p-W	p-AFS	p-W/p- AFS
1	1198.7 hm <sup>2</sup>	43.3 hm <sup>2</sup>	27.7	3328.1 hm <sup>2</sup>	135.2 hm <sup>2</sup>	24.6
2	0 hm <sup>2</sup>	0 hm <sup>2</sup>	-	4786.4 hm <sup>2</sup>	878.34 hm <sup>2</sup>	5.5
3	14116.4 hm <sup>2</sup>	1271.6 hm <sup>2</sup>	11.1	15846.26 hm <sup>2</sup>	1918.46 hm <sup>2</sup>	8.3
4	573.9 hm <sup>2</sup>	50.7 hm <sup>2</sup>	11.3	1271.4 hm <sup>2</sup>	95.7 hm <sup>2</sup>	13.3
3,2	26.2 hm <sup>2</sup>	1.3 hm <sup>2</sup>	20.2	0 hm <sup>2</sup>	0 hm <sup>2</sup>	-
5	153.9 hm <sup>2</sup>	39.9 hm <sup>2</sup>	3.9	264.4 hm <sup>2</sup>	39.9 hm <sup>2</sup>	6.6
6	26.4 hm <sup>2</sup>	1.5 hm <sup>2</sup>	17.6	322.1 hm <sup>2</sup>	33.4 hm <sup>2</sup>	9.6
7	82.7 hm <sup>2</sup>	9.3 hm <sup>2</sup>	8.9	82.7 hm <sup>2</sup>	9.3 hm <sup>2</sup>	8.9
8	53.8 hm <sup>2</sup>	5.6 hm <sup>2</sup>	9.6	53.8 hm <sup>2</sup>	5.6 hm <sup>2</sup>	9.6
9	241.5 hm <sup>2</sup>	12.1 hm <sup>2</sup>	20.0	181.2 hm <sup>2</sup>	12.1 hm <sup>2</sup>	15.0
10	65.7 hm <sup>2</sup>	8.9 hm <sup>2</sup>	7.4	125.2 hm <sup>2</sup>	8.9 hm <sup>2</sup>	14.1



11	19.6 hm <sup>2</sup>	5.1 hm <sup>2</sup>	3.8	359.1 hm <sup>2</sup>	15.2 hm <sup>2</sup>	23.6
12	0 hm <sup>2</sup>	0 hm <sup>2</sup>	-	174.5 hm <sup>2</sup>	15.6 hm <sup>2</sup>	11.2
13	172.5 hm <sup>2</sup>	16.2 hm <sup>2</sup>	10.6	0 hm <sup>2</sup>	0 hm <sup>2</sup>	-
14	0 hm <sup>2</sup>	0 hm <sup>2</sup>	-	7456.7 hm <sup>2</sup>	421.6 hm <sup>2</sup>	17.7
15	0 hm <sup>2</sup>	0 hm <sup>2</sup>	-	9310.0 hm <sup>2</sup>	549.6 hm <sup>2</sup>	16.9
16	797.5 hm <sup>2</sup>	22.9 hm <sup>2</sup>	34.8	797.5 hm <sup>2</sup>	42.3 hm <sup>2</sup>	18.9
17	0 hm <sup>2</sup>	0 hm <sup>2</sup>	-	7661 hm <sup>2</sup>	987 hm <sup>2</sup>	7.8

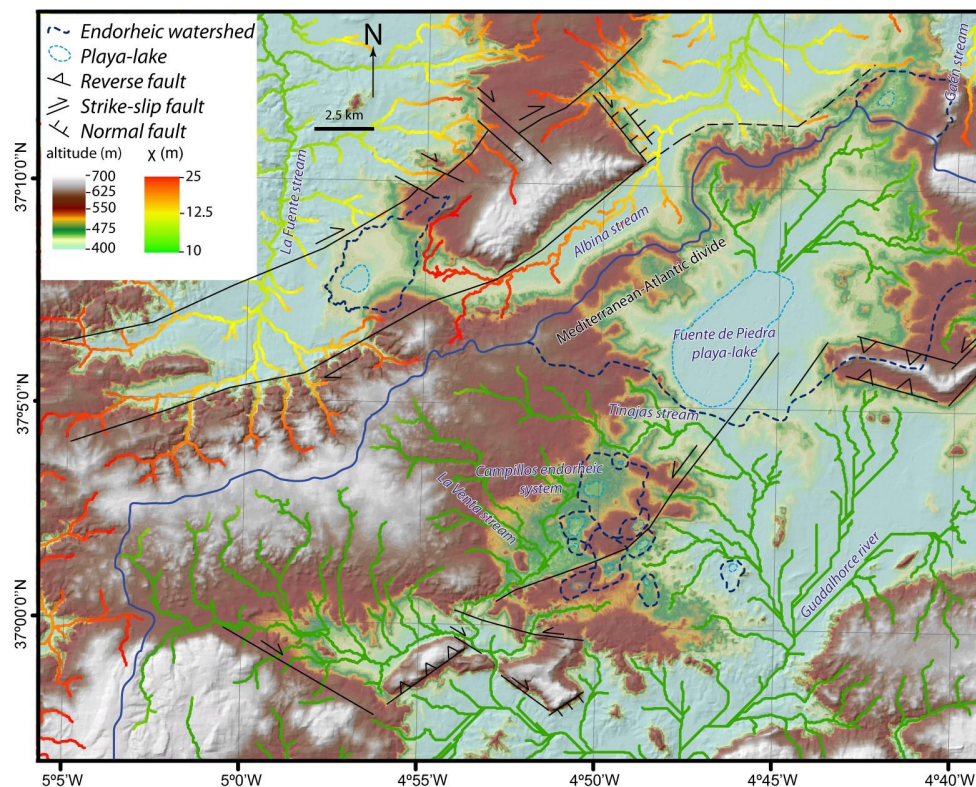
432

433

434           The  $\chi$  map shows significant contrasting values across the Atlantic-Mediterranean  
435 water divide (Fig. 8). Guadalhorce tributaries are characterized by very low values at their  
436 headwaters ( $\chi < 12.5$  m) whilst Guadalquivir tributaries always show  $\chi > 20$  m at their headwaters.



437



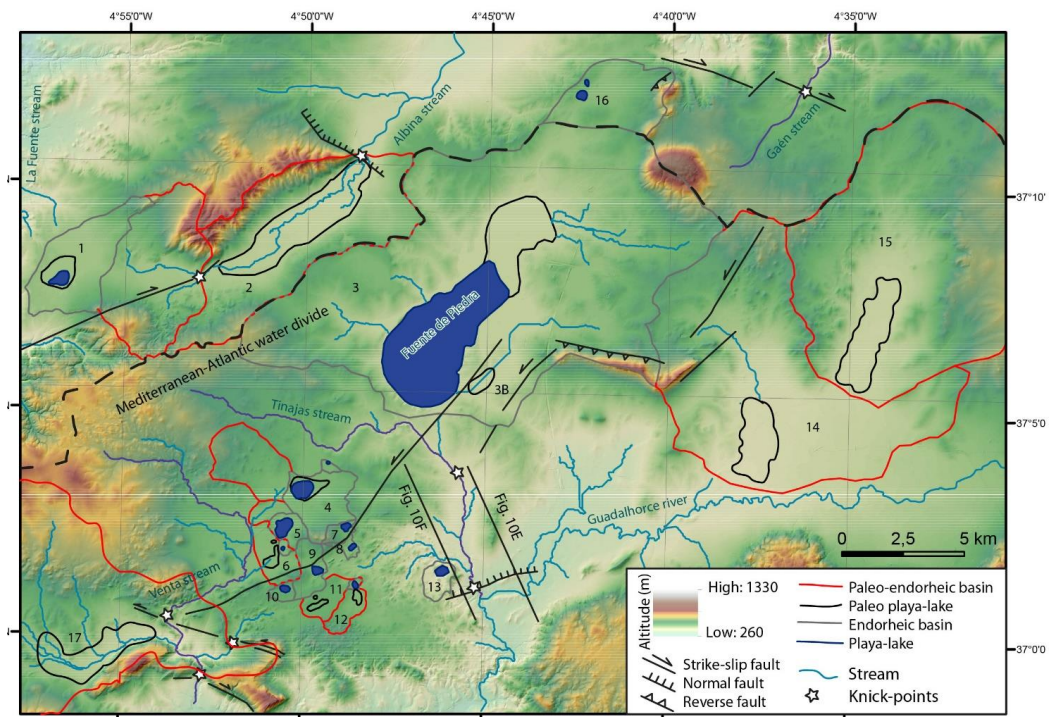
438

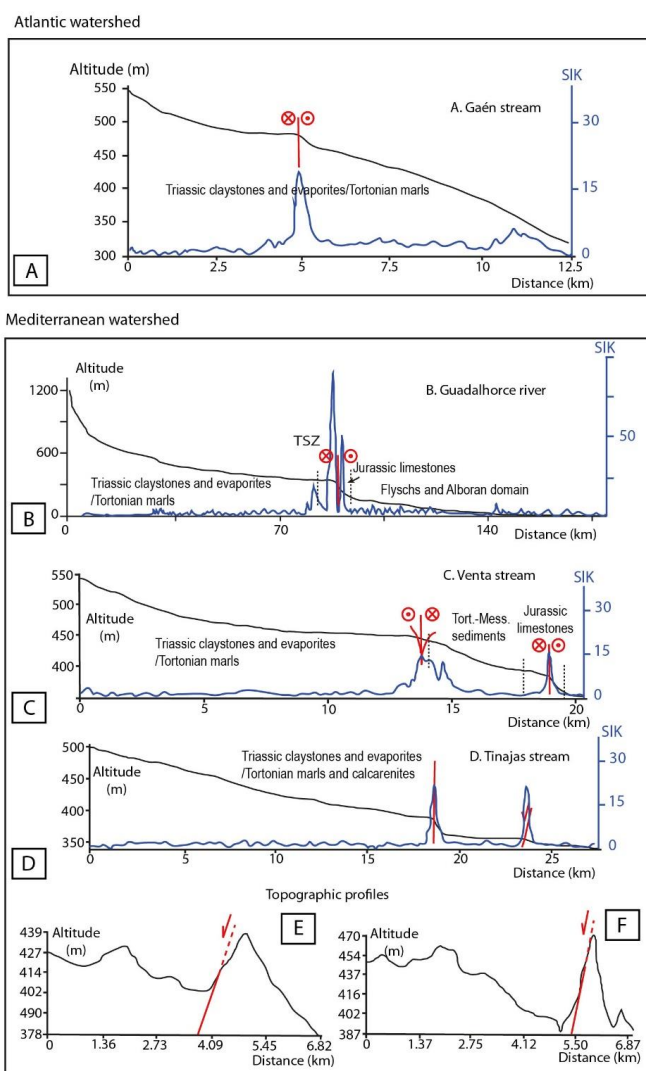
439 Fig. 8:  $\chi$  map together with the DEM showing the main playa-lake systems and post-  
440 Serravallian structures (Junta de Andalucía, 2016; modified from Jiménez-Bonilla et al., 2023).  
441 See location in Fig. 2.

442 Regarding the Atlantic watershed, previous studies analysed the captures of basins 1 and  
443 2 by the Albino stream and La Fuente stream (Jiménez-Bonilla et al., 2023; Figs. 8 and 9). In  
444 order to complete the analysis of this watershed, we have performed the long profile and the SLk  
445 index for the Gaén stream (Figs. 9 and 10A). The long profile shows two different stream  
446 segments: a concave segment, which extends for approximately 5 km from the source, and a  
447 slightly convex profile with a higher gradient, located downstream. Both stream segments are  
448 separated by a knick-point, higher than 20 m, that is related to a SLk value greater than 15 (Fig.  
449 10A).



450





454

455 Fig. 10. (A), (B), (C) and (D) stream and SIK profiles of main rivers of the Atlantic (Gaén stream)

456 and Mediterranean (Guadalhorce, Venta and Tinajas stream) watersheds within the studied area.

457 (E) and (F) topographic profiles parallel to the Tinajas stream. See Fig. 9 for location of streams.

458

459 In general, Mediterranean streams frequently show steeper gradients than Guadalquivir

460 tributaries. In the studied area, the main Guadalhorce river exhibits an elbow geometry in plan

461 view (Figs. 1 and 2). Two kilometers downstream of the elbow there is a knick-point and an SIK



462 value of more than 75, which is related to the capture of the upper Guadalorce watershed (at 85  
463 km from the source; Fig. 10B). The Guadalorce segment that runs through the ADA, upstream  
464 of the Guadalorce capture, shows a flat stream long profile and it flows on thick alluvial deposits  
465 (Figs. 5A and 10B). Downstream of the knickpoint, the stream profile shows a steeper gradient,  
466 and the river is deeply incised into the limestones of the TSZ.

467 More in detail, we also analyse the Tinajas and the la Venta streams (Figs. 10C and 10D),  
468 which discharge in the Guadalorce river upstream of its capture (Figs. 1, 2 and 9).

469 The La Venta stream is an antecedent river that crosses perpendicularly the western TSZ  
470 (Fig. 2A, 6D and 9). Its long profile is characterized by the presence of two knickpoints, located  
471 at 13 and 19 km, which show SLk values higher than 10 (Fig. 10C). The La Venta stream shows  
472 a concave profile from its source down to the first knick-point. This knick-point spatially  
473 coincides with two post-Tortonian fault zones (Figs. 5A, 6A and 10C). The stream segment  
474 between both knick-points shows a higher slope and it is characterized by a gorge deeply incised  
475 into the Jurassic limestones of the western TSZ (Fig. 6D). The knick-point located at 19 km is  
476 related to a post-Tortonian dextral strike-slip fault. This knick-point builds up a waterfall > 10 m  
477 high (Fig. 10C) with an associated 5-10 m thick tufa outcrop, located at 420 m a.s.l., and dated at  
478 9,000 BP (Comino and Senciales, 2012). Additionally, there are many cavities in the Peñarrubia  
479 range that worked as phreatic conducts. These conducts are currently preserved upper than 100 m  
480 from the phreatic surface, within the vadose zone, thus supporting the hypothesis of the recent  
481 uplift of the western TSZ.

482 To the E of the La Venta stream head there are 9 playa-lakes (endorheic basins 4 to 12;  
483 Fig. 9 and Table 2) that constitute the Campillos endorheic system. Playa-lakes 4, 6, 11 and 12  
484 show a significant decrease on their AFS during the Pleistocene to Holocene, which is related to  
485 water input reduction because of W reduction, as suggested by roughly constant W/AFS ratios  
486 (Table 2). Other playa-lakes increased their W and AFS (e.g. playa-lake 9: Fig. 9 and Table 2).  
487 By contrast, W and AFS pairs of playa-lakes 7 and 8 remained steady during the last thousands



488 of years (Fig. 9 and Table 2). To the W of the La Venta stream we have mapped the paleo playa-  
489 lake 17. It is a depressed area with a flat topography and filled by moor sediments.

490 From headwater to mouth, the Las Tinajas stream changes its trend from W-E to NW-SE  
491 and finally to N-S close to the mouth (Fig. 9). The stream profile also shows two knickpoints  
492 close to the mouth: at 19 and 24 km, which show SLk values higher than 15 (Fig. 10D). As the  
493 La Venta stream, it shows a concave geometry from the source down to the first knick-point (Fig.  
494 10D). This stream segment is characterized by low erosion rates (concave stream segment) and  
495 thick quaternary alluvial terraces. The biggest playa-lake in this area, the Fuente de Piedra playa-  
496 lake, is only 800 m to the N of this stream segment (playa-lake 3). Although the W sector of this  
497 playa-lake seems to remain steady during the Holocene, its AFS was likely reduced (from approx.  
498 1900 hm<sup>2</sup> to 1300 hm<sup>2</sup>; Fig. 9 and Table 2). From 19 to 24 km the stream profile shows a flat  
499 geometry and alluvial terraces were deposited during the Holocene. Close to this stream segment  
500 the playa-lake 13 developed (Table 2 and Fig. 9). The knick-point located at ca. 24 km spatially  
501 coincides with normal faults previously described (Figs. 5A, 5E and 9). This knick-point is also  
502 associated with a gorge, > 5 m high (Fig. 10D). When topographic profiles are drawn parallel to  
503 the stream profiles, we observe that this knick-point is associated with a topographic escarpment  
504 SW-NE (Figs. 9, 10E and 10F).

505 Endorheic basins 14 and 15 developed along the Guadalorce river right bank, upstream  
506 of the Tinajas stream outlet (Fig. 9 and Table 2). Although they are currently drained by a channel  
507 network used for agriculture purposes, endorheic basin 14 was captured by the Guadalorce  
508 during the Holocene whilst endorheic basin 15 was not.

509

## 510 **7. Discussion**

511 To understand the birth of internally drained basins and the Atlantic-Mediterranean watershed  
512 divide migration is important to identify the mechanisms that controlled the upper Miocene  
513 differential surface uplift and how it controls the recent evolution the Western Gibraltar Arc. Our



514 results will be put in context together with data from previous works that account for some of  
515 these processes.

516

### 517 **7.1. Role of transpressional tectonics on the ADA inception**

518 First evidence of emersion in the study area dates from the upper Miocene. The upper  
519 Miocene coastline has been mapped in previous works by detecting Tortonian and Messinian  
520 abrasion platform borders (Elez et al., 2016; Braga et al., 2003; Fig. 11). Its current position shows  
521 that the central TSZ was probably uplifted at the late Tortonian more than 500 m above the sea  
522 level. This uplift was probably favoured by the transpressional activity at this zone. However,  
523 depressed parts of this barrier, associated with relay zones between shear zone segments, likely  
524 allowed to localize the Atlantic-Mediterranean communication through the Guadalhorce gateway  
525 (Figs. 1 and 11). The activity of the TSZ along the Messinian continuously raised this topographic  
526 barrier, finally closing the Guadalhorce gateway at 6.2 My (Fig. 11). This, together with the  
527 closure of the other gateways between the Atlantic Ocean and the Mediterranean Sea, isolated the  
528 latter (Roveri et al, 2014). Because of its negative water balance, the sea level in the  
529 Mediterranean Sea sharply dropped more than 1000 m, giving place to the Mediterranean Salinity  
530 Crisis (MSC; Martín et al., 2001; Blanc, 2006; Madof et al., 2019), whilst the sea level in the  
531 Atlantic watershed maintained. This is illustrated by the Mediterranean stream incision on upper  
532 Miocene outcrops that originated deep gorges in the Messinian (Elez et al., 2016; 2020). Despite  
533 the high stream power erosion of Mediterranean streams, this divide remained stable at the TSZ  
534 until the Pliocene (Elez et al., 2016 and this work), probably due to the Messinian tectonic activity  
535 of the TSZ as we have observed in this work. Instead, the Mediterranean Sea reopened to the  
536 Atlantic by means of the Gibraltar strait, which provoked the Zanclean flood at 5.33 My (Roveri  
537 et al., 2014) and the levelling of both watersheds. This opening was probably favoured by the  
538 existence of E-W trending faults located in the strait area (Luján et al., 2011).



539           There is consensus about the importance of post-Tortonian uplift in the western Betics.  
540 Previous works , based on geomorphology models, attributed 50-55% of the upper Miocene uplift  
541 (or all post-Messinian uplift) observed in the Guadalhorce watershed to an isostatic rebound,  
542 produced by differential erosion rates between Atlantic and Mediterranean watersheds provoked  
543 by the sea level drop in the Mediterranean watershed, a direct consequence of the MSC (Farines  
544 et al., 2015; Elez et al., 2016, 2020). However, according to the model assumptions, these  
545 estimations are valid in the orogen-scale but do not consider differential uplifting at different  
546 sectors and/or specific structures within the Atlantic-Mediterranean divide area. The results  
547 presented here in combination with some of our previous works (Díaz-Azpiroz et al., 2014;  
548 Barcos et al., 2015) fill this gap. In the study area, Tortonian-Messinian sediments, deposited  
549 close to the sea level, were uplifted up to 610 m in the western segment of the TSZ and up to 850  
550 in the central TSZ (part of the current Mediterranean watershed; Fig. 3). These are 200-450 m  
551 higher than the same sediments in the ADA. This range contains theoretical post-Tortonian  
552 uplifting values calculated through a transpressional kinematic model using specific combinations  
553 compatible with the TSZ activity (Fig. 7). Therefore, our results indicate that transpression at the  
554 TSZ with moderate strain rate values (likely resulting in total contraction between 0.09 and 0.11),  
555 roughly constant since the Messinian, would suffice to explain the observed differential uplift  
556 with respect to the depressed sector of the study area. Moreover, our structural results do not  
557 account for the elongate domal structure required by Elez et al. (2016, 2020) models.

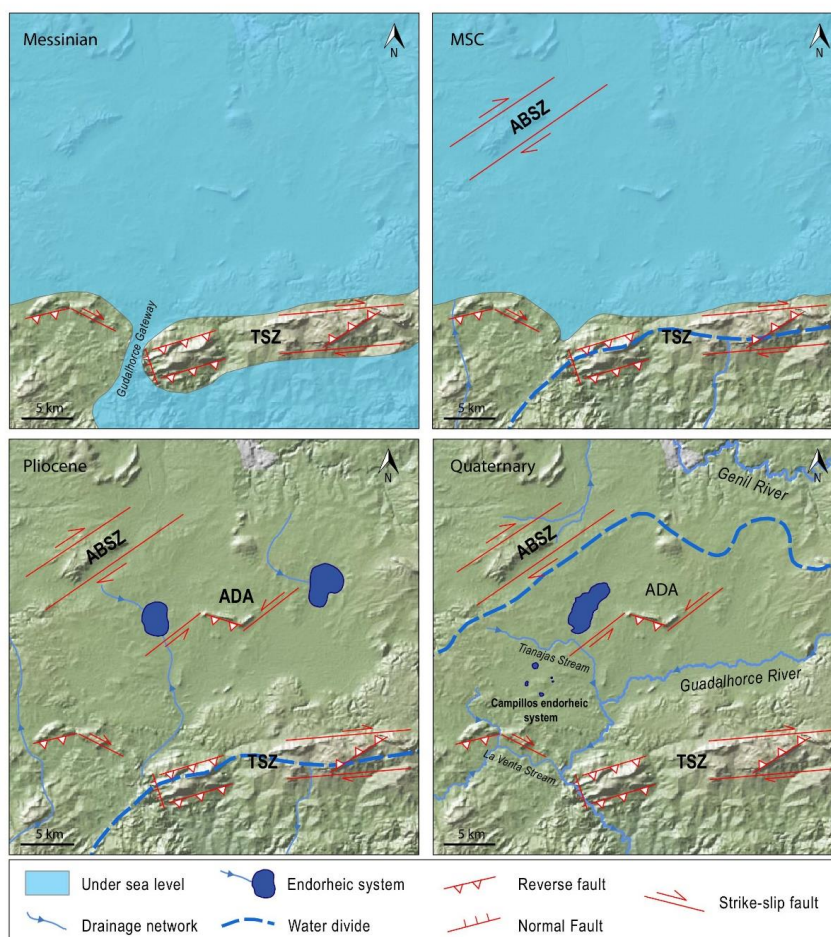
558           In contrast with irrelevant uplift values reported previously for the Atlantic watershed  
559 (Elez et al., 2016; 2020), we also observed significant uplift in this watershed, especially related  
560 to the ABSZ. The differential surface uplift of the ABSZ compared to less deformed areas in the  
561 ADA would reach around 200 m. Unlike the TSZ, which partially emerged during the Tortonian,  
562 there is no evidence of ABSZ emersion until the Messinian (Elez et al., 2016). There are indeed  
563 Messinian sedimentary depocenters within the ABSZ (Fig. 5A, see also Jiménez-Bonilla et al.,  
564 2015). However, the current relief shows that some segments of the ABSZ reach 750 m (Fig. 9).  
565 These arguments suggest that the ABSZ tectonic activity, although kinematically similar to that



566 of the TSZ, would start later. This is congruent with a diachronic migration of the deformation  
567 towards the foreland during fold-and-thrust belts evolution (e.g. Davis et al., 1983). Once the  
568 ABSZ emerged, the ADA individualized (Fig. 11). The age of the complete emersion of the ADA  
569 is not completely constrained. First homogeneous continental deposits (Pliocene conglomerates)  
570 overlay Messinian sediments, so emersion should have occurred at some point within the Pliocene  
571 (from 5 to 2.5 My). Moreover, first lake sediments, which are probably related to endorheic  
572 basins, are Pliocene in age (Medina 1991).

573 Both the TSZ and ABSZ accommodate the western Gibraltar arc protrusion, which is still  
574 active (Balanyá et al., 2012). The presence of earthquakes close to the ABSZ (e.g. Ruíz-Costán  
575 et al., 2012; Díaz-Azpiroz et al., 2022) and geomorphic analyses in the ABSZ and TSZ (e.g.  
576 Barcos et al., 2015; Jiménez-Bonilla et al., 2015 and this work) suggest that both shear zones are  
577 still active.

578 Consequently, although we do not discard a moderate post-Messinian uplift on the  
579 Mediterranean watershed, especially south of the TSZ, due to an isostatic rebound, our work  
580 highlights the importance of dextral transpressional bands on the generation of differential uplift  
581 within the fold-and-thrust belt (even in the Atlantic watershed).



583 Fig. 11. Block diagram of the ADA inception and evolution (same area as in Fig. 3). We show  
584 the drainage network, water divide, mountain building and endorheic watershed evolution from  
585 Messinian to Quaternary (Junta de Andalucía, 2016).

586

## 587 7.2. Atlantic-Mediterranean water divide migration and the development of endorheic 588 watersheds

589 The Atlantic-Mediterranean water divide originated during the Messinian Guadalhorce  
590 gateway closure, and was coincident with the TSZ (Figs. 2 and 11). This water divide must have



591 been maintained close to the TSZ during the ADA continentalization as indicated by the Pliocene  
592 sediments north of the wTSZ: The source of these Pliocene conglomerates is the Alboran domain,  
593 which is farther S nowadays. It means that during the Pliocene, the flow direction was from the  
594 Alboran domain to the N, thus suggesting that this area was drained by Atlantic rivers. Nowadays,  
595 this area belongs to the Mediterranean watershed (From 5 to 1 My; Figs. 1, 2 and 5A). To the E  
596 of the ADA, there are some Pliocene lacustrine deposits (Medina, 1991; Vera, 2004).  
597 Consequently, endorheic watersheds were probably established since the ADA formed and they  
598 were close to the Atlantic-Mediterranean water divide at the Pliocene (Fig. 11).

599         The water divide would have therefore migrated NW-ward during the Quaternary (Figs.  
600 2 and 11). This migration coincides spatially and temporarily with the outward propagation of the  
601 transpressive deformation front, accommodated by the ABSZ and TSZ. The Mediterranean  
602 capture of the ADA by the Guadalhorce river and its tributaries was probably favoured by the  
603 ABSZ related surface uplift, that blocked other northward possible captures, and the coeval NW-  
604 SE normal faults within the TSZ that depressed specific, narrow zones, such as those near the  
605 Guadalhorce course (Barcos et al., 2015).

606         Going to the recent evolution of the ADA, a crucial question is the evolution of current  
607 playa-lakes close to the Atlantic-Mediterranean water divide. Playa-lakes *stricto sensu*, as we  
608 described in sections 1 and 2, probably developed during the Early Pleistocene, but due to their  
609 ephemeral lifespan, they disappeared or/and were reshaped and their sediments probably  
610 eroded. The earliest age obtained for current playa-lakes associated with endorheic basins is of  
611 30 ky in the Fuente de Piedra playa-lake (Late Pleistocene; Högig et al., 2016). Previous works  
612 have pointed out that since endorheic systems were formed, they were strongly conditioned by  
613 climatic changes and human modifications because of their weak equilibrium between water  
614 inputs and outputs (Rodríguez-Rodríguez et al., 2007; 2012). As we observed, the large number  
615 of playa-lakes preserved in the ADA is probably favoured by the most recent uplifts caused by  
616 both the TSZ and ABSZ and their respective tip zones, which shaped a roughly triangular closed  
617 zone that contains all the studied cases (see sections 4 and 5; Fig. 2) and act as relief barriers that



618 prevent erosion from the Atlantic and Mediterranean streams (Fig. 2). Additionally, active  
619 tectonics in this sector may also influence the shrinkage or disappearance of some endorheic  
620 watersheds hosting playa-lakes because of the reduction of the overall water input due to stream  
621 captures (Figs. 3, 9 and Table 2; Jiménez-Bonilla et al., 2023).

622           The long lifespan of some playa-lakes such as Fuente de Piedra (30 Ky; Höbig et al.,  
623 2016) is probably conditioned by active tectonics. The dip-slip movement of the left-lateral  
624 dominated fault of the transverse zone within the ADA (see section 4.3) located at the E boundary  
625 of this playa-lake could have prevented this playa-lake capture, despite being located only about  
626 1 km away from the upper course of the Las Tinajas stream, a tributary of the Guadalhorce (Table  
627 2 and Fig. 5A; see also  $\chi$  values on Fig. 8 and Fig. 9). Moreover, the Fuente de Piedra paleo-AFS  
628 would be bigger and it would include playa-lake 3B and 3 (Fig. 9 and Table 2). This left-lateral  
629 dominated fault would have splitted the playa-lake into two. The eastern one (playa-lake 3B) is  
630 separated by a topographic high with respect to its parental lake and it is located at 5 m higher  
631 than the current Fuente de Piedra bottom lake (Table 2 and Fig. 9).

632           In contrast, some playa-lake systems are the result of this recent activity, as the playa-  
633 lake 13, nucleated on the downthrown, northern wall of a WSW-ENE normal fault intersecting  
634 the lower course of the Las Tinajas stream (Fig 9). This stream is deeply incised into the bedrock  
635 in the uplifted southern wall of that fault.

636           Regarding the Campillos endorheic system (playa-lakes 4 to 12), its evolution seems to  
637 be conditioned by the balance between the western TSZ segment uplift and the headward erosion  
638 capacity of the La Venta stream. Although the La Venta stream is an antecedent river, as indicated  
639 by its strong incision (Fig. 6D), its upper course could have been transiently disconnected from  
640 the drainage network due to the uplift of western TSZ during the Quaternary. This disconnection  
641 probably formed an endorheic area where the Campillos endorheic system and paleo playa-lake  
642 17 developed (Fig. 9 and Table 2). The age of this endorheic basin development is not well  
643 constrained. Nevertheless, the age of the travertine associated with the wTSZ uplift (9,000 years  
644 old, see section 6) must pre-date the recapture of playa-lake 17 as well as part of the paleo-playa-



645 lakes of the Campillos endorheic system (Table 2). The partial preservation of this system would  
646 be due to the recent activity of a left-lateral dominated transpressive fault, located to the NE of  
647 the western TSZ. This fault together with all the structures related to this tip generate a relief  
648 barrier which slows down the migration of the knick-point upstream (Fig. 10C). It is also  
649 congruent with the relative uplift observed in the upper Miocene rocks of the western TSZ with  
650 respect to the ADA (Fig. 3). If the tectonic activity stopped at the western TSZ, the Campillos  
651 endorheic system would likely be captured in some hundred years. Other partial or complete  
652 captures of endorheic watersheds have been observed N of the Campillos endorheic system during  
653 the last 2,000 years (playa-lakes 1 and 2; Table 2; Recio-Ruíz and Ruiz-Somavilla, 1990;  
654 Jiménez-Bonilla et al., 2023). In this case, an Atlantic watershed river completely captured playa-  
655 lake 2 and partially playa-lake 1 because of the active tectonics of central ABSZ (Jiménez-Bonilla  
656 et al., 2023; Table 2; Fig. 9).

657           Although predictions of the future development of playa-lakes is speculative, some  
658 guidelines can be made. Mediterranean streams are aggressor streams, so they should capture part  
659 of endorheic basins and even Atlantic streams according to their lower  $\chi$  values (Fig. 8). However,  
660 Mediterranean streams show really low incision capacity at their headwaters showing thick river  
661 terraces, open valleys and poor development of their drainage networks. The presence of knick-  
662 points along stream profiles is frequently favoured by active discrete faults that provoke relative  
663 uplift. Thus, although the Atlantic-Mediterranean water divide will probably move NW-ward,  
664 endorheic basins will develop, hosted between the ABSZ and the TSZ, within the ADA (Figs. 5,  
665 8, 9 and 11). This work shows the study of a water divide movement and drainage integration of  
666 endorheic basins settled in a transpressional tectonic setting, which is complementary with  
667 previous works made in other tectonic settings: extensional settings (Repasch et al., 2017; Berry  
668 et al., 2019), foreland basins (Anton et al., 2014), intramontane basins (Giano and Schiattarella,  
669 2023) and contractional belts (Sobel et al., 2003; Willett et al., 2014).

670

## 671 **8. Conclusions**



672           In this work, we study a depressed area (ADA), limited by the TSZ and the ABSZ, to the  
673 S and to the N, respectively, within the Betics fold-and-thrust belt to delve into the Atlantic-  
674 Mediterranean water divide evolution from the Messinian to the Quaternary. This water divide is  
675 currently diffuse, and it is characterized by the presence of many endorheic watersheds. We  
676 combined structural and hydro - geomorphic analysis: we collected kinematic data from faults  
677 active during the last 5 My and we analysed the drainage network and endorheic watersheds using  
678 geomorphic indexes such as SLk and  $\chi$ .

679           We observed differences on the post-Tortonian surface uplift within the study area that  
680 are congruent with the tectonic activity of both the TSZ and the ABSZ. Consequently, structures  
681 must be considered in studies of orogenic uplift in the Betics. The relative uplift built up by these  
682 shear zones condition the relief evolution and the drainage network development:

- 683       - The early uplift of the TSZ probably conditioned the Guadalhorce gateway closure and it  
684       did not reopen even though the high erosion power of Mediterranean streams during the  
685       Messinian Salinity Crisis (MSC). The TSZ uplift controlled the location and geometry of  
686       the Pliocene Atlantic-Mediterranean water divide.
- 687       - The ABSZ tectonic activity would start later than the TSZ, which suggests a migration of  
688       the deformation towards the foreland at this fold-and-thrust belt segment. This migration  
689       of the deformation probably conditioned the Quaternary migration of the Atlantic-  
690       Mediterranean water divide.
- 691       - The tectonic activity of both transpressive zones (the TSZ and the ABSZ) generated the  
692       ADA, where many endorheic watersheds develop from the Pliocene to Holocene. The  
693       recent tectonic activity of faults associated with TSZ and ABSZ prevents the capture of  
694       these endorheic watersheds from streams, especially those draining to the Mediterranean  
695       Sea. The kinematics of active faults may condition the evolution of playa-lakes  
696       (movement, split, diminution or increase of its average flooded area).

697   **Author contributions**



698 AJB led the research and wrote the draft. AJB and MDA made analyses. MDA, AJB, MRR,  
699 IE, JLY and JCB participated in the fieldwork for both qualitative geomorphological analysis  
700 and structural analysis. All the authors participated in the results interpretation and in the text  
701 improvement.

#### 702 **Competing interests**

703 The contact author has declared that none of the authors has any competing interests.

#### 704 **Acknowledgements**

705 We thank the keepers of the Natural Reserve of Lagunas de Campillos and Fuente de Piedra  
706 for support during field surveys. This study was supported by the research projects: PGC2018-  
707 100914-B-I00, UPO-1259543, “Monitorización hidrológica y modelización de la relación  
708 laguna-acuífero en los mantos eólicos de Doñana” of the Ministerio de Economía y  
709 Competitividad of Spain, Fondo Europeo de Desarrollo Regional FEDER and Guadalquivir River  
710 Basin Authority and “Tectonic conditioning and climate change effects on the hydrogeological  
711 evolution of wetlands and playa-lakes in the southern Spain” from the University of Pablo de  
712 Olavide.

713

#### 714 **References**

715 Aguirre, J., Braga, J. C., Martín-Pérez, J. A., Martín, J. M. and Puga-Bernabéu, Á., 2022. Upper  
716 Miocene deposits at the southern margin of the Guadalquivir Foreland Basin (central Betic  
717 Cordillera, S. Spain). Implications for the closure timing of the Atlantic-Mediterranean  
718 connections. *Revue de Micropaléontologie*, 76, 100690.

719 <https://doi.org/10.1016/j.revmic.2022.100690>

720 Andreo, B., Gil-Márquez, J. M., Mudarra, M., Linares, L. and Carrasco, F., 2016. Hypothesis on  
721 the hydrogeological context of wetland areas and springs related to evaporitic karst aquifers



- 722 (Málaga, Córdoba and Jaén provinces, Southern Spain). *Environmental Earth Sciences*, 75, 1-  
723 19. <https://doi.org/10.1007/s12665-016-5545-1>
- 724 Antón L., De Vicente G., Muñoz-Martin A., Stokes M. (2014). Using river profiles and  
725 geomorphic indices to evaluate geomorphological signature of continental scale drainage  
726 capture, Duero basin (NW Spain). *Geomorphology*, 206, 250-261,  
727 <https://doi.org/10.1016/j.geomorph.2013.09.028>
- 728 Babault, J., Van Den Driessche, J. and Teixell, A., 2012. Longitudinal to transverse  
729 drainage network evolution in the High Atlas (Morocco): The role of tectonics.  
730 *Tectonics*, 31(4). <https://doi.org/10.1029/2011TC003015>
- 731 Balanyá, J. C., Crespo-Blanc, A., Díaz Azpiroz, M., Expósito, I. and Luján, M., 2007. Structural  
732 trend line pattern and strain partitioning around the Gibraltar Arc accretionary wedge: insights as  
733 to the mode of orogenic arc building. *Tectonics*, 26(2). <https://doi.org/10.1029/2005TC001932>
- 734 Balanya, J. C., Crespo-Blanc, A., Díaz-Azpiroz, M., Expósito, I., Torcal, F., Pérez-Peña, V. and  
735 Booth-Rea, G. (2012). Arc-parallel vs back-arc extension in the Western Gibraltar arc: Is the  
736 Gibraltar forearc still active?. *Geologica Acta: an international earth science journal*, 10(3), 249-  
737 263.
- 738 Barcos, L., Balanyá, J. C., Díaz-Azpiroz, M., Expósito, I., & Jiménez-Bonilla, A. (2015). Kinematics  
739 of the Torcal Shear Zone: Transpressional tectonics in a salient-recess transition at the northern  
740 Gibraltar Arc. *Tectonophysics*, 663, 62-77. <https://doi.org/10.1016/j.tecto.2015.05.002>
- 741 Barcos, L., Díaz-Azpiroz, M., Balanyá, J. C., Expósito, I., Jiménez-Bonilla, A. and Faccenna, C.,  
742 2016. Analogue modelling of inclined, brittle–ductile transpression: testing analytical models  
743 through natural shear zones (external Betics). *Tectonophysics*, 682, 169-185.  
744 <https://doi.org/10.1016/j.tecto.2016.05.021>
- 745 Berry M., Wijk J. van, Emry E., García-Castellanos D. (2019). Endorheic-Exorheic transitions of  
746 the Río Grande and East African Rifts. *Geochemistry, Geophysics and Geosystems*, 20, 3705-  
747 3729, <https://doi.org/10.1029/2018GC008176>



- 748 Blanc, P. L., 2006. Improved modelling of the Messinian Salinity Crisis and conceptual  
749 implications. *Palaeogeography, Palaeoclimatology, Palaeoecology*, 238(1-4), 349-372.  
750 <https://doi.org/10.1016/j.palaeo.2006.03.033>
- 751 Braga, J. C., Martín, J. M. and Quesada, C., 2003. Patterns and average rates of late Neogene–  
752 Recent uplift of the Betic Cordillera, SE Spain. *Geomorphology*, 50(1-3), 3-26.  
753 [https://doi.org/10.1016/S0169-555X\(02\)00205-2](https://doi.org/10.1016/S0169-555X(02)00205-2)
- 754 Calaforra, J. M. and Pulido-Bosch, A., 1999. Gypsum karst features as evidence of diapiric  
755 processes in the Betic Cordillera, Southern Spain. *Geomorphology*, 29(3-4), 251-264.  
756 [https://doi.org/10.1016/S0169-555X\(99\)00019-7](https://doi.org/10.1016/S0169-555X(99)00019-7)
- 757 Comino, J., and Senciales, J.M., 2012. Las plataformas travertínicas y tobáceas de la provincia  
758 de Málaga (España). *Baetica. Estudios de Arte, Geografía e Historia*, 34, 2012, 83-102.
- 759 Davis, D., Suppe, J. and Dahlen, F. A., 1983. Mechanics of fold-and-thrust belts and  
760 accretionary wedges. *Journal of Geophysical Research: Solid Earth*, 88(B2), 1153-  
761 1172. <https://doi.org/10.1029/JB088iB02p01153>
- 762 Díaz-Azpiroz, M., Barcos, L., Balanyá, J. C., Fernández, C., Expósito, I. and Czeck, D.  
763 M., 2014. Applying a general triclinic transpression model to highly partitioned brittle-  
764 ductile shear zones: A case study from the Torcal de Antequera massif, external Betics,  
765 southern Spain. *Journal of Structural Geology*, 68, 316-336.  
766 <https://doi.org/10.1016/j.jsg.2014.05.010>
- 767 Díaz Azpiroz, M., Asencio Almansa, R., Senín Andrades, J. R., & Jiménez Bonilla, A. 2020. Shape  
768 preferred orientation of dolostone bodies of a Triassic broken formation at the western External  
769 Betics.
- 770 Díaz-Azpiroz, M., Jiménez-Bonilla, A., Frontera, T., Expósito, I. and Balanyá, J.C., (2022). Strain  
771 partitioning at the active mountain front of the western Betics (southern Spain). European Society  
772 for Deformation Mechanisms, Rheology and Tectonics. DRT 2022. Catania.



- 773 Elez, J., Silva, P. G., Huerta, P., Perucha, M. Á., Civis, J., Roquero, E. and Martínez-Graña, A.,  
774 2016. Quantitative paleotopography and paleogeography around the Gibraltar arc (South Spain)  
775 during the Messinian salinity crisis. *Geomorphology*, 275, 26-45.  
776 <https://doi.org/10.1016/j.geomorph.2016.09.023>
- 777 Elez, J., Silva, P. G., Huerta, P. and Martínez-Graña, A., 2018. Isostatic compensation in the  
778 Western-Central Betic Cordillera (South Spain) caused by erosional unloading from the Messinian  
779 to the present: the emergence of an orogen. *Geogaceta*, 64, 103-106.
- 780 Elez, J., Silva, P. G. and Martínez-Graña, A. M., 2020. Quantification of Erosion and Uplift in a  
781 Rising Orogen—A Large-Scale Perspective (Late Tortonian to Present): The Case of the Gibraltar  
782 Arc, Betic Cordillera, Southern Spain. *Remote Sensing*, 12(21), 3492.
- 783 England, P. and Molnar, P., 1990. Surface uplift, uplift of rocks, and exhumation of rocks.  
784 *Geology*, 18(12), 1173-1177. [https://doi.org/10.1130/0091-](https://doi.org/10.1130/0091-7613(1990)018<1173:SUUORA>2.3.CO;2)  
785 [7613\(1990\)018<1173:SUUORA>2.3.CO;2](https://doi.org/10.1130/0091-7613(1990)018<1173:SUUORA>2.3.CO;2)
- 786 Ercilla, G., Juan, C., Periáñez, R., Alonso, B., Abril, J. M., Estrada, F. and Valencia, J., 2019.  
787 Influence of alongslope processes on modern turbidite systems and canyons in the Alboran Sea  
788 (southwestern Mediterranean). *Deep Sea Research Part I: Oceanographic Research Papers*,  
789 144, 1-16. <https://doi.org/10.1016/j.dsr.2018.12.002>
- 790 Expósito, I., Jiménez-Bonilla, A., Delchiaro, M., Yanes, J. L., Balanyá, J. C., Moral-Martos, F. and  
791 Della Seta, M., 2022. Geomorphic signature of segmented relief rejuvenation in the Sierra  
792 Morena, Betic forebulge, Spain. *Earth Surface Dynamics*, 10(5), 1017-1039.  
793 <https://doi.org/10.5194/esurf-10-1017-2022>
- 794 Expósito, I., Balanyá, J. C., Crespo-Blanc, A., Díaz-Azpiroz, M. and Luján, M., 2012. Overthrust  
795 shear folding and contrasting deformation styles in a multiple decollement setting, Gibraltar Arc  
796 external wedge. *Tectonophysics*, 576, 86-98. <https://doi.org/10.1016/j.tecto.2012.04.018>
- 797 Farines, B., Calvet, M., & Gunnell, Y. (2015). The summit erosion surfaces of the inner Betic  
798 Cordillera: Their value as tools for reconstructing the chronology of topographic growth in  
799 southern Spain. *Geomorphology*, 233, 92-111.  
800 <https://doi.org/10.1016/j.geomorph.2014.11.019>



- 801 Fernandez, C., Czeck, D. M., & Diaz-Azpiroz, M. (2013). Testing the model of oblique  
802 transpression with oblique extrusion in two natural cases: steps and consequences. *Journal of*  
803 *Structural Geology*, 54, 85-102. <https://doi.org/10.1016/j.jsg.2013.07.001>
- 804 Fuentes, P., Fernández, C., Díaz-Alvarado, J. and Díaz-Azpiroz, M., 2019. Using 3D kinematic  
805 models in subduction channels. The case of the Chañaral tectonic mélangé, Coastal Cordillera,  
806 northern Chile. *Gondwana Research*, 74, 251-270. <https://doi.org/10.1016/j.gr.2018.12.009>
- 807 Garcia-Alix, A., Jimenez-Moreno, G., Gazquez, F., Monedero-Contreras, R., López-Avilés, A.,  
808 Jimenez-Espejo, F. J., ... & Anderson, R. S. (2022). Climatic control on the Holocene hydrology  
809 of a playa-lake system in the western Mediterranean. *Catena*, 214, 106292.  
810 <https://doi.org/10.1016/j.catena.2022.106292>
- 811 Giano S.I. and Schiattarella M. (2023). Drainage integration of small endorheic basins at the  
812 Pleistocene-Holocene transition: An example from southern Italy. *Geomorphology*, 427,  
813 <https://doi.org/10.1016/j.geomorph.2023.108622>
- 814 Gil-Márquez, J. M., Barberá, J. A., Andreo, B. and Mudarra, M., 2017. Hydrological and  
815 geochemical processes constraining groundwater salinity in wetland areas related to evaporitic  
816 (karst) systems. A case study from Southern Spain. *Journal of Hydrology*, 544, 538-554.  
817 <https://doi.org/10.1016/j.jhydrol.2016.11.062>
- 818 Giletycz, S., Loget, N., Chang, C. P. and Mouthereau, F., 2015. Transient fluvial landscape and  
819 preservation of low-relief terrains in an emerging orogen: example from Hengchun Peninsula,  
820 Taiwan. *Geomorphology*, 231, 169-181. <https://doi.org/10.1016/j.geomorph.2014.11.026>
- 821 Harkins, N., Kirby, E., Heimsath, A., Robinson, R. and Reiser, U., 2007. Transient fluvial incision  
822 in the headwaters of the Yellow River, northeastern Tibet, China. *Journal of Geophysical*  
823 *Research: Earth Surface*, 112(F3). <https://doi.org/10.1029/2006JF000570>
- 824 Höbig, N., Mediavilla, R., Gibert, L., Santisteban, J. I., Cendón, D. I., Ibáñez, J. and Reicherter,  
825 K., 2016. Palaeohydrological evolution and implications for palaeoclimate since the Late Glacial  
826 at Laguna de Fuente de Piedra, southern Spain. *Quaternary International*, 407, 29-46.  
827 <https://doi.org/10.1016/j.quaint.2016.02.051>



- 828 Jiménez Bonilla, A., Barcos, L., Expósito, I., Balanyá, J. C. and Díaz Azpiroz, M., 2013. La Zona  
829 Transversal de Peñarrubia-Almargen (Béticas): tectónica transpresiva tardía y segmentación del  
830 relieve. *Geogaceta* 55, 7-10.
- 831 Jiménez-Bonilla, A., Expósito, I., Balanyá, J. C., Díaz-Azpiroz, M. and Barcos, L., 2015. The role  
832 of strain partitioning on intermontane basin inception and isolation, External Western Gibraltar  
833 Arc. *Journal of Geodynamics*, 92, 1-17. <https://doi.org/10.1016/j.jog.2015.09.001>
- 834 Jiménez-Bonilla, A., Expósito, I., Balanyá, J. C., & Díaz-Azpiroz, M., 2017. Strain partitioning and  
835 relief segmentation in arcuate fold-and-thrust belts: a case study from the western Betics. *Journal*  
836 *of Iberian Geology*, 43, 497-518. <https://doi.org/10.1007/s41513-017-0028-0>
- 837 Jiménez-Bonilla, A., Díaz-Azpiroz, M., Rodríguez, M. R. (2023). Tectonics may affect closed  
838 watersheds used to monitor climate change and human activity effects. *Terra Nova*, 35(1), 58-  
839 65. <https://doi.org/10.1111/ter.12629>
- 840 Jiménez-Bonilla, A., Crespo-Blanc, A., Balanyá, J. C., Expósito, I. and Díaz-Azpiroz, M., 2020.  
841 Analog models of fold-and-thrust wedges in progressive arcs: a comparison with the Gibraltar Arc  
842 external wedge. *Frontiers in Earth Science*, 8, 72.
- 843 Junta de Andalucía, 2016. ([http://www.](http://www.juntadeandalucia.es/institutodeestadisticaycartografia/prodCartografia/bc/mdt.htm)  
844 [juntadeandalucia.es/institutodeestadisticaycartografia/prodCartografia/bc/mdt.htm](http://www.juntadeandalucia.es/institutodeestadisticaycartografia/prodCartografia/bc/mdt.htm))
- 845 Keller, G. R., 1986. Introduction to special section on the Rio Grande rift. *Journal of Geophysical*  
846 *Research: Solid Earth*, 91(B6), 6142-6142.
- 847 Keller, E. A. and Pinter, N., 1996. *Active tectonics* (Vol. 338). Upper Saddle River, NJ: Prentice  
848 Hall.
- 849 Korup, O., 2006. Rock-slope failure and the river long profile. *Geology*, 34(1), 45-48.  
850 <https://doi.org/10.1130/G21959.1>
- 851 Lhénaff, R. (1967). *Recherches Geomorphologiques sur les cor Dilleres Betiques Centre*  
852 *accidentales* (Doctoral dissertation, PhD. thesis, Univ. de Lille 1, Villeneuve d'Ascq, France).



- 853 Loget, N. and Van Den Driessche, J., 2006. On the origin of the Strait of Gibraltar. *Sedimentary*  
854 *Geology*, 188, 341-356. <https://doi.org/10.1016/j.sedgeo.2006.03.012>
- 855 Luján, M., Crespo-Blanc, A. and Comas, M., 2011. Morphology and structure of the Camarinal  
856 Sill from high-resolution bathymetry: evidence of fault zones in the Gibraltar Strait. *Geo-Marine*  
857 *Letters*, 31, 163-174. <https://doi.org/10.1007/s00367-010-0222-y>
- 858 Madof, A. S., Bertoni, C. and Lofi, J., 2019. Discovery of vast fluvial deposits provides evidence  
859 for drawdown during the late Miocene Messinian salinity crisis. *Geology*, 47(2), 171-174.  
860 <https://doi.org/10.1130/G45873.1>
- 861 Martín, J. M., Braga, J. C. and Betzler, C., 2001. The Messinian Guadalhorce corridor: the last  
862 northern, Atlantic–Mediterranean gateway. *Terra Nova*, 13(6), 418-424.  
863 <https://doi.org/10.1046/j.1365-3121.2001.00376.x>
- 864 Martín, J. M., Braga, J. C., Aguirre, J. and Puga-Bernabéu, Á., 2009. History and evolution of the  
865 North-Betic Strait (Prebetic Zone, Betic Cordillera): a narrow, early Tortonian, tidal-dominated,  
866 Atlantic–Mediterranean marine passage. *Sedimentary Geology*, 216(3-4), 80-90.  
867 <https://doi.org/10.1016/j.sedgeo.2009.01.005>
- 868 Martín Martín, J. M., Puga Bernabeu, Á., Aguirre Rodríguez, J. and Braga Alarcón, J. C., 2014.  
869 Miocene Atlantic-Mediterranean seaways in the Betic Cordillera (Southern Spain).
- 870 Mather A.E. (2000). Adjustment of a drainage network to capture induced base-level change:  
871 an example from the Sorbas Basin, S. Spain. *Geomorphology*, 34, 271-289.  
872 [https://doi.org/10.1016/S0169-555X\(00\)00013-1](https://doi.org/10.1016/S0169-555X(00)00013-1)
- 873 Medialdea, T., Suriñach, E., Vegas, R., Banda, E. and Ansorge, J., 1986. Crustal structure under  
874 the western end of the Betic Cordillera (Spain). In *Annales geophysicae. Series B. Terrestrial and*  
875 *planetary physics* (Vol. 4, No. 4, pp. 457-464).
- 876 Medina, F. C. (1991). Mapa Geológico de España E. 1: 50.000.



- 877 Pérez-Peña, J. V., Azañón, J. M., Azor, A., Delgado, J., & González-Lodeiro, F. (2009). Spatial  
878 analysis of stream power using GIS: SLk anomaly maps. *Earth Surface Processes and*  
879 *Landforms*, 34(1), 16-25. <https://doi.org/10.1002/esp.1684>
- 880 Pérez-Peña, J. V., Azor, A., Azañón, J. M. and Keller, E. A. (2010). Active tectonics in the Sierra  
881 Nevada (Betic Cordillera, SE Spain): Insights from geomorphic indexes and drainage pattern  
882 analysis. *Geomorphology*, 119(1-2), 74-87. <https://doi.org/10.1016/j.geomorph.2010.02.020>
- 883 Perron, J. T. and Royden, L., 2013. An integral approach to bedrock river profile analysis. *Earth*  
884 *surface processes and landforms*, 38(6), 570-576.
- 885 <https://doi.org/10.1002/esp.3302>
- 886 Recio-Ruiz, A. and Ruíz-Somovilla, I., 1990. Prospecciones arqueológicas en el T.M. de Sierra  
887 de Yeguas (Málaga). *Prospecciones arqueológicas*, 11- 12, 93–110.
- 888 Repasch M., Karlstrom K.E., Heizler M., Pecha M. (2017). Birth and evolution of the Rio Grande  
889 fluvial system in the past 8 Ma: Progressive downward integration and the influence of tectonics,  
890 volcanism, and climate. *Earth-Science Reviews*, 168, 113-164.  
891 <https://doi.org/10.1016/j.earsci.2017.03.003>
- 892 Rodríguez-Rodríguez, M., 2007. Hydrogeology of ponds, pools, and playa-lakes of southern  
893 Spain. *Wetlands*, 27(4), 819-830.
- 894 Rodríguez-Rodríguez, M., Moral, F. and Benavente, J. 2009. Grado de dependencia de las aguas  
895 subterráneas, índice de funcionamiento hidrológico y principales amenazas en los principales  
896 humedales continentales de la depresión del Guadalquivir. *Boletín Geológico y Minero*, 120(3),  
897 347-360.
- 898 Rodríguez-Rodríguez, M., Moral, F., Benavente, J. and Beltrán, M., 2010. Developing  
899 hydrological indices in semi-arid playa-lakes by analyzing their main morphometric, climatic and  
900 hydrochemical characteristics. *Journal of Arid Environments*, 74(11), 1478-1486.  
901 <https://doi.org/10.1016/j.jaridenv.2010.03.018>
- 902 Rodríguez-Rodríguez, M., Green, A. J., López, R. and Martos-Rosillo, S., 2012. Changes in water  
903 level, land use, and hydrological budget in a semi-permanent playa lake, Southwest Spain.



- 904 *Environmental Monitoring and Assessment*, 184, 797-810. <https://doi.org/10.1007/s10661->  
905 011-2002-1
- 906 Rodriguez-Rodriguez, M., Martos-Rosillo, S. and Pedrera, A., 2016. Hydrogeological behaviour  
907 of the Fuente-de-Piedra playa lake and tectonic origin of its basin (Malaga, southern Spain).  
908 *Journal of Hydrology*, 543, 462-476. <https://doi.org/10.1016/j.jhydrol.2016.10.021>
- 909 Roveri, M., Flecker, R., Krijgsman, W., Lofi, J., Lugli, S., Manzi, V. and Stoica, M., 2014. The  
910 Messinian Salinity Crisis: past and future of a great challenge for marine sciences. *Marine*  
911 *Geology*, 352, 25-58. <https://doi.org/10.1016/j.margeo.2014.02.002>
- 912 Ruiz-Constán, A., Pedrera, A., Galindo-Zaldívar, J., Pous, J., Arzate, J., Roldán-García, F. J.  
913 and Anahnah, F., 2012. Constraints on the frontal crustal structure of a continental collision from  
914 an integrated geophysical research: The central-western Betic Cordillera (SW Spain).  
915 *Geochemistry, Geophysics, Geosystems*, 13(8). <https://doi.org/10.1029/2012GC004153>
- 916 Sanderson, D. J., & Marchini, W. R. D. (1984). Transpression. *Journal of structural Geology*, 6(5),  
917 449-458. [https://doi.org/10.1016/0191-8141\(84\)90058-0](https://doi.org/10.1016/0191-8141(84)90058-0)
- 918 Sanz de Galdeano, C. and Alfaro, P., 2004. Tectonic significance of the present relief of the Betic  
919 Cordillera. *Geomorphology*, 63(3-4), 175-190. <https://doi.org/10.1016/j.geomorph.2004.04.002>
- 920 Schoorl, J. M. and Veldkamp, A., 2003. Late Cenozoic landscape development and its tectonic  
921 implications for the Guadalhorce valley near Alora (Southern Spain). *Geomorphology*, 50(1-3),  
922 43-57. [https://doi.org/10.1016/S0169-555X\(02\)00207-6](https://doi.org/10.1016/S0169-555X(02)00207-6)
- 923 Schulmann, K., Thompson, A. B., Lexa, O. and Ježek, J., 2003. Strain distribution and fabric  
924 development modeled in active and ancient transpressive zones. *Journal of Geophysical*  
925 *Research: Solid Earth*, 108(B1), ETG-6.  
926 <https://doi.org/10.1029/2001JB000632>  
927
- 928 Sobel E.R., Hillel G.E., Strecker M.R. (2003). Formation of internally drained contractional basins  
929 by aridity-limited bedrock incision. *Journal of Geophysical Research*, 108,  
930 <https://doi.org/10.1029/2002JB001883>



- 931 Stokes M., Mather A.E., Kearsey S.H., Lewin S. (2019). Anatomy, Age and Origin of an  
932 Intramontane Top Basin Surface (Sorbas Basin, Betic Cordillera, S. Spain). *Quaternary*, 1, 15,  
933 <https://doi.org/10.3390/quat1020015>
- 934 Torné, M. and Banda, E., 1992. Crustal thinning from the Betic Cordillera to the Alboran Sea.  
935 *Geo-Marine Letters*, 12, 76-81. <https://doi.org/10.1007/BF02084915>
- 936 Vera, J. A., 2004. Geología de España. Instituto Geológico y Minero de España (IGME), Madrid,  
937 884 p. *Geology of Spain*".
- 938 Whipple, K. X. and Tucker, G. E., 1999. Dynamics of the stream-power river incision model:  
939 Implications for height limits of mountain ranges, landscape response timescales, and research  
940 needs. *Journal of Geophysical Research: Solid Earth*, 104(B8), 17661-17674.  
941 <https://doi.org/10.1029/1999JB900120>
- 942 Willett, S. D., McCoy, S. W., Perron, J. T., Goren, L. and Chen, C. Y., 2014. Dynamic  
943 reorganization of river basins. *Science*, 343(6175), 1248765. DOI: [10.1126/science.1248765](https://doi.org/10.1126/science.1248765)
- 944 Winterberg, S. and Willett, S. D., 2019. Greater Alpine river network evolution, interpretations  
945 based on novel drainage analysis. *Swiss Journal of Geosciences*, 112, 3-22.  
946 <https://doi.org/10.1007/s00015-018-0332-5>